International Journal of Mechanical Sciences 318 (2026) 111546

Contents lists available at ScienceDirect

International Journal of Mechanical Sciences

journal homepage: www.elsevier.com/locate/ijmecsci

# Confinement mechanisms governed by stiffness contrast in auxetic cementitious composites

Zhaozheng Meng [a,*], Yading Xu [a,b,c], Wen Zhou [a,d], Rowin J.M. Bol [a], Jinbao Xie [a], Branko Šavija [a]

[a] Microlab, Faculty of Civil Engineering and Geosciences, Delft University of Technology, Stevinweg 1, 2628 CN Delft, the Netherlands
[b] College of Materials Science and Engineering, Chongqing University, Chongqing, 400045, China
[c] State Key Laboratory of Safety and Resilience of Civil Engineering in Mountain Area, Chongqing, 400045, China
[d] School of Civil and Environmental Engineering, Nanyang Technological University, 50 Nanyang Avenue, 639798, Singapore

ARTICLE INFO

*Keywords:*
Cementitious composites
Additive manufacturing
Mechanical behavior
Auxetic lattices
Stiffness contrast
Confinement mechanism

ABSTRACT

This study systematically investigates the role of lattice–matrix stiffness contrast in governing confinement and mechanical performance of cementitious composites reinforced by 3D-printed auxetic (negative Poisson's ratio) lattices. Through combined compression testing, numerical simulations, and representative volume element (RVE) analysis, the mechanistic link between stiffness ratio and macroscopic response is established. The results demonstrate that sufficient stiffness contrast is a prerequisite for activating auxetic-induced confinement, enabling the translation of lattice lateral contraction into effective confinement on the cementitious matrix. Auxetic cementitious composites with 3D-printed steel lattice achieved a compressive strength exceeding 80 MPa (nearly 300% higher than plain mortar and polymer lattice reinforced composites). The specific energy absorption was 90% greater than the theoretical sum of the steel lattice and matrix, owing to the strong confinement and synergy enabled by the stiffness contrast. In contrast, polymer lattice reinforced composites, despite possessing the same geometry and similar negative Poisson's ratios, exhibited limited confinement efficiency as the low stiffness suppressed the transfer of auxetic deformation to matrix. RVE analyses revealed that the stiffness contrast between the lattice and matrix governs the mesoscale confinement behavior, which in turn influences the macroscopic strength, ductility, and energy dissipation capacity of auxetic cementitious composites. These findings establish stiffness contrast as the governing design parameter for auxetic cementitious composites and provide a basis for tailoring architected cementitious composites.

## 1. Introduction

Concrete is the most widely used construction materials nowadays due to their excellent load-bearing capacity, cost-effectiveness, and adaptability to various construction conditions [1,2]. Advancements in recent decades have transformed conventional concrete into a family of engineered composite materials incorporating fibers [3,4], supplementary cementitious materials [5,6], and other polymers [7,8], enabling enhanced mechanical performance, durability, environmental sustainability, and even functionality [9,10]. This evolution underscores the ongoing advancement of materials engineering in cementitious systems, which has progressively shifted from empirical mixture design toward the rational tailoring of composition, geometry, and microstructure to achieve desired mechanical and functional performance [11,12]. Through these engineered approaches, modern cementitious composites are being designed as tailorable, adaptive, and multifunctional materials meeting the complex performance requirements of next-generation infrastructure [13,14].

Recent advances in additive manufacturing have further expanded the design possibilities of cementitious composites [15,16]. One of the applications is lattice-reinforced cementitious composites, where the 3D-printed architected lattice structures with different properties are embedded in cementitious matrices to offer tailored responses beyond what can be achieved through compositional modification alone [17,18]. Among the diverse lattice architectures explored, auxetic lattices with negative Poisson's ratios (NPR) have emerged as a promising reinforcement [19–21]. The auxetic behavior, characterized by lateral contraction under compression, is primarily achieved through the

* Corresponding author.
*E-mail address:* z.meng@tudelft.nl (Z. Meng).

https://doi.org/10.1016/j.ijmecsci.2026.111546
Received 2 January 2026; Received in revised form 27 February 2026; Accepted 25 March 2026
Available online 25 March 2026

geometric design of the lattice structure, where local deformation of lattice joints or hinges introduces an overall negative Poisson's ratio [22,23]. Typical auxetic topologies include re-entrant, chiral, rotating square, and star-shaped lattices, in which their local deformation commits to the global contraction [24,25]. Because of this unconventional NPR behavior, the lateral contraction from lattice structures could lead to a confinement effect of the surrounded matrix [26,27]. As a result, the biaxial or triaxial confinement provided from the auxetic lattice could enhance the toughness, energy absorption, and structural stability of the composite system [28–30].

The mechanical behavior of auxetic lattice structures has been extensively investigated over the past decades [31,32]. One important line of development involves the design of hybrid auxetic architectures that integrate multiple deformation mechanisms to enhance mechanical performance [33,34]. Hu et al. [35] developed hybrid auxetic lattice structures based on re-entrant structures, and reported that the designed structure showed better performance under tension. Yang et al. [36] innovatively integrated multiple auxetic mechanism and designed auxetic structures that can maintain negative Poisson's ratio strain range of 0.8 under compression. Luo et al. found that by using face-centered cubic cells in re-entrant structures, the high stiffness can be harnessed as reinforcement to stabilize the deformation under compression [37]. Hybrid lattice structures have been explored as multifunctional materials [38]. For example, hybrid metamaterials incorporating triply periodic minimal surface and resonant units have also been developed to be applicable for both vibration attenuation and load-bearing purposes [39]. In addition to the hybrid structure design, multi-material 3D printing has also been widely employed to fabricate auxetic materials with enhanced and tunable mechanical performance [40,41]. To maximize deformation at the lattice joints, elastic materials are often employed for the joint regions, while the lattice beams were printed using a stiffer material [42]. It has been reported that single-material auxetic lattices exhibit superior performance under monotonic loading, whereas dual-material configurations perform better under cyclic loading, as elastic buckling enables enhanced energy absorption [43]. Several other studies have adopted an assembly-based approach to design multi-material auxetic lattice structures, where the advantages extend beyond improved mechanical performance to include demountability and reusability [44,45]. Although recent advances in additive manufacturing have enabled the manufacturing of complex auxetic topologies, their mechanical response remains highly sensitive to the specific fabrication process adopted [46,47]. For example, Maskery et al. [48] demonstrated that selective laser melting could induce porosity and geometric imperfections that strongly influence the compressive response of lattice structures. Wauthle et al. [49] also reported similar results that build orientation and heat treatment can have a significant impact on the mechanical properties of 3D-printed lattice structures. In fused deposition modeling method, significant variations in mechanical properties of auxetic structures can be caused by different printing orientations [50], and researchers showed that a printing direction aligned with the loading direction can offer the best strength and ductility [51]. Moreover, residual stresses and microstructural heterogeneity generated during powder-bed fusion processes have also been shown to alter the failure mechanisms of architected lattices [52,53]. Consequently, manufacturability constraints have been proposed to guide the practical design and reliable application of additively manufactured lattice structures [54].

In addition to the progress in design and manufacturing of auxetic materials, extensive efforts have also been devoted to elucidating the mechanical performance and underlying mechanisms of cementitious composites with auxetic lattice reinforcements [55,56]. Studies using soft polymer-based auxetic lattice reinforcement have shown that the brittle failure behavior can be effectively prevented, and shearing damage of cementitious matrix can be also inhibited due to auxeticity of the lattice reinforcement [57]. The initial stiffness and peak strength under uniaxial compression were reduced due to the incorporation of polymer phase within the stiffer cementitious matrix, but the contribution of ductile lattice structures was more pronounced under bending conditions [58,59]. For instance, Bol et al. [60] developed tailored Poisson's ratio reinforcement in cementitious composites, and the results showed these polymer-based reinforcement could significantly enhance the load-bearing capacity and toughness under bending. Furthermore, stiffer polymers such as polylactic acid (PLA) have also been employed to reinforce ultra-high-performance concrete (UHPC), and the results demonstrated that the strength was improved compared with the reference specimens in some specific types of auxetic architecture [61]. Recently, re-entrant auxetic lattices fabricated by dual material were employed as reinforcement inside cementitious matrix, and it showed that the connection types between the two materials would have a significant influence on the properties of cementitious composites [62]. According to the authors' previous research, polymer-based auxetic lattices exhibited a limited confinement effect on the cementitious matrix at the early loading stage due to the large stiffness disparity between the lattice and the matrix, i.e. the reinforcement being significantly less stiff than the matrix [63]. However, as progressive damage developed within the matrix, the auxetic deformation of the polymer lattice became more active, contributing significantly to the enhancement of post-peak ductility and energy absorption capacity [64]. Auxetic lattice reinforcement has also been used to improve dynamic behaviors of cementitious composites [65]. Gan et al. [66] developed auxetics textile reinforced mortar composites which showed outperformed stress-damping capacities at higher strain rates. The low speed impact test also showed that compared to reference samples, cementitious composites reinforced by auxetic textiles showed increased fracture energy up to 20 times [67].

Apart from polymer-based auxetic lattice, metallic auxetic lattice structures were also investigated due to their higher stiffness and load-bearing capacities [68,69]. Hamed et al. [70] studied the auxetic steel plate shear walls, and it showed that the out-of-plane buckling can be significantly reduced. Wang et al. [71] utilized perforated steel plate in auxetic shape as shear walls, where no pinching effect was observed for the hysteresis behavior under cyclic loading. Liu et al. [72] studied the eccentric compression performance of auxetic structures by combined selective laser melting and bolt-welding assembly strategy. The results showed that the metallic hybrid auxetic structure outperformed traditional re-entrant under eccentric compression. Zhou et al. [68] investigated the in-plane impact behavior of re-entrant auxetic structures fabricated from 3D-printed stainless steel and reported that the auxetic configurations exhibited superior energy absorption capacity compared with their non-auxetic counterparts. Besides, some scholars also reported temperature-dependent properties for metallic auxetic structures manufactured by 3D printing techniques [73]. For example, Papadakis et al. [74] showed that heat treatment can improve the mechanical properties of selective laser melting printed auxetic lattice structures, highlighting the role of post-processing in controlling the mechanical properties of metallic auxetic materials. Beyond their role as structural components, auxetic structures have also been widely studied as reinforcement in cementitious composites [75,76]. Zhong et al. [77] infilled aluminum auxetic honeycomb structures with cement mortar, and results showed that the post-peak ductility can be improved while shear-dominated failing pattern was still observed. The study by Zhou et al. [78] revealed that the auxeticity of auxetic reinforced foam concrete decreased with increasing compression velocity. Tzortzinis et al. [79] manufactured steel-based auxetic lattice structures using selective laser melting method, and concluded that the auxetic lattice could exert an active confinement over the matrix and improve the compressive strength by 140%. Luo et al. [80] developed a concrete-filled auxetic tube composite structure and reported that the auxetic architecture can prevent outward local buckling of the composite tube due to negative Poisson ratio effect. The simulation conducted by Yang et al. [81] showed that concrete reinforced by 3D auxetic structures showed more significant confinement, while the 2D auxetic reinforced concrete

showed higher strength. Most recently, Vandadi et al. [82] printed auxetic lattice structures using three different base materials including PLA, aluminum, and stainless steel featuring distinctively different stiffnesses and strengths, and compared the auxetic lattice-reinforced composites with fiber-reinforced composites and plain mortar. Their results showed that for composites reinforced by auxetic lattices printed by PLA, nearly all designs had lower strength and ductility than the fiber-reinforced concrete samples, although some exhibited slightly better ductility than the plain mortar. When aluminum was used as the base material, some auxetic lattices achieved higher strength and ductility than the fiber-reinforced concrete, while others were weaker but still outperformed the plain mortar. In contrast, when steel was used as the base material, almost all auxetic cementitious composites performed better than the fiber-reinforced samples.

From the abovementioned literature review, it can be noticed that existing studies have demonstrated the potential of auxetic lattice reinforcements to enhance the ductility, energy absorption, and post-peak behavior of cementitious composites. However, the mechanical properties of such composites are strongly influenced by the stiffness contrast between the auxetic lattice and the cementitious matrix, which governs the confinement degree, stress transfer efficiency, and damage evolution process. Furthermore, although the enhanced mechanical performance of auxetic cementitious composites is often attributed to the confinement effect induced by auxetic deformation, experimental or numerical evidence supporting this mechanism remains limited. Most importantly, the underlying mechanisms governing the mechanical interaction within lattice-reinforced cementitious composite systems, as well as the role of constituent mechanical properties in determining the overall behavior of the composites, have not been systematically clarified. Developing a more fundamental understanding of these interactions is essential for establishing reliable design principles for auxetic cementitious composites and promoting their application as a new class of high-performance, architected construction materials.

This study aims to address this research gap by conducting a combined experimental and numerical investigation on cementitious composites reinforced with auxetic lattices 3D-printed by materials with distinctively different mechanical properties (i.e., polymer and steel). The auxetic lattices were manufactured using fused filament fabrication method, where the steel auxetic lattice was successfully manufactured by this technique for the first time. Uniaxial compression tests were conducted to evaluate the macroscopic mechanical behavior, while digital image correlation was used to capture local strain evolution and experimentally reveal the confinement strain fields induced by auxetic behavior, which were further confirmed through finite element simulations. Moreover, to better understand the influencing mechanism of stiffness contrast in composite systems, representative volume element analyses with periodic boundary conditions were performed to derive the homogenized elastic properties of the orthotropic composite system. The insights obtained from this study provide a more in-depth understanding of two-component lattice-reinforced cementitious composites and offer guidance for the rational design of architected cement-based materials with tailored stiffness, ductility, and energy dissipation characteristics.

## 2. Experimental tests

This section presents the experimental framework to investigate the mechanical response of auxetic lattice-reinforced cementitious composites. The materials used for 3D printing and cementitious mixture adopted in the study are first introduced, followed by the fabrication process of both standalone lattices and composite specimens. Subsequently, the mechanical test setup, including uniaxial compression loading configuration and Digital Image Correlation (DIC) measurements, is then outlined.

### 2.1. Materials and manufacturing

The steel auxetic lattices were 3D printed using BASF Ultrafuse 17–4 pH stainless steel filament via fused filament fabrication (FFF) method. According to the manufacturer, the annealed material exhibits a tensile strength ranging from 1276 MPa to 1319 MPa, depending on different printing directions. The maximum elongation lies between 6% and 7%, and the elastic modulus is reported to be between 198 GPa and 202 GPa, also depending on the printing directions. The lattice structures were manufactured by UltiMaker S5 3D printer under the dual-extrusion mode, with BASF Ultrafuse Support Layer filament serving as the support material. The main printing parameters, as recommended by the manufacturer, are summarized in Table 1. After printing, the samples were post-processed by Elnik Systems for subsequent debinding and sintering. To compare the influence of different constituent stiffness contrasts on the mechanical properties of the composites, polymer-based auxetic lattices were also manufactured by using Acrylonitrile Butadiene Styrene (ABS), the printing parameters are also shown in Table 1. Compared to the 3D printed steel, the ABS showed much lower stiffness (between 1.7 GPa and 1.9 GPa) and yielding strength (approximately 38 MPa) [83].

Cement mortar was used as the matrix material, where CEM I 42.5 N cement, fly ash, and fine sand with a particle size ranging between 0.125 mm and 0.250 mm were used as the dry material. In addition, polycarboxylate-based superplasticizer (Glenium 51) was added to improve the workability. This mortar mix design was selected to ensure sufficient flowability for the complete infiltration of the lattice reinforcements, thereby avoiding voids or incomplete filling during casting. The detailed mixture proportions have been listed in Table 2. It should be noted that the mortar used in this study had a water-to-cement ratio of 0.4 and exhibited sufficient flowability to infiltrate the lattice structures during casting. Nevertheless, the flowability of the mortar remains a critical parameter influencing manufacturability and interfacial quality, and should be considered in practical applications.

### 2.2. Sample preparation

Fig. 1(a) illustrates the geometric design of the auxetic lattices, where the auxetic behavior was achieved through a “rotating square” mechanism [84]. In the planar arrangement, two-unit cells were positioned along both the vertical and horizontal directions. The strut width of the lattice structure was designed as 1.2 mm, while the overall in-plane dimensions were 38 mm × 38 mm with a thickness of 10 mm. The total volume of the designed auxetic lattice was approximately 3915 $mm^3$. The detailed design parameters and geometry representation for single unit cell are described in Appendix A. After 3D-printing, steel auxetic lattices were subjected to debinding (removing thermoplastic binder) and sintering (fusing metal particles) to obtain fully dense metallic parts. In contrast, polymeric lattices fabricated using ABS were utilized directly without further post-processing. The processed lattice structures were subsequently embedded into the prepared molds prior to casting of the cementitious matrix.

The cement mortar was prepared by first mixing the dry materials for 2 min, followed by the addition of water and an additional 2 min of mixing. The slurry was then cast into the mold and vibrated for 15 s to

**Table 1**
Printing parameters for BASF Ultrafuse 17–4 pH filament and ABS filament.

| Parameters | Ultrafuse 17–4 pH metal filament | ABS polymer filament |
|---|---|---|
| Nozzle size | 0.4 mm | 0.4 mm |
| Layer thickness | 0.15 mm | 0.15 mm |
| Wall thickness | 0.8 mm | 0.8 mm |
| Infill density | 105% | 100% |
| Material flow | 100 % | 120% |
| Printing speed | 25 mm/s | 100 mm/s |

**Table 2**
Mixture proportions of cementitious matrix (kg/m$^3$).

| Cement | Fly ash | Sand (0.125~0.250 mm) | Water | Superplasticizer |
|---|---|---|---|---|
| 473 | 559 | 473 | 413 | 2 |

ensure a uniform distribution inside the lattice unit cells. The steel auxetic lattice reinforced composite samples were demolded 48 h after casting and subsequently cured under a temperature of 20 ± 2 °C and a relative humidity of 96 ± 2% until reaching an age of 28 days. Each specimen had dimensions of 40 mm × 40 mm × 10 mm, with a total of three duplicate samples prepared for each lattice configuration. In addition, reference specimens without lattice reinforcement were fabricated for comparison.

### 2.3. Test setup

Uniaxial compression tests were conducted on auxetic lattices (both steel and ABS) and cementitious composites to evaluate the mechanical properties. A constant strain rate of 2.5 × $10^{-4}$ $s^{-1}$ (corresponding to a loading rate of 0.01 mm/s) was applied, and the total loading displacement was set to 12.0 mm, corresponding to a compressive strain of 30% relative to the specimen height. Plastic foils lubricated with oil were placed between the specimen and the loading plates to reduce the boundary friction. Two linear variable differential transformers (LVDTs) were placed between two loading plates to measure the compressive deformation. Furthermore, digital image correlation analysis was conducted to capture the deformation of the auxetic cementitious composites during loading. A Canon EOS 6D Mark II digital camera was positioned 600 mm away from the specimen surface to acquire high-resolution images throughout the test. The camera was equipped with a 75 mm focal length lens and operated at an aperture of *f*/2.8. Images were captured at a resolution of 6240 × 4160 pixels. The composite samples were painted with a white background and sprayed with black speckle patterns to ensure optimal contrast and accuracy in DIC measurements.

## 3. Numerical model

In this section, a finite element model simulating the mechanical behaviors of auxetic cementitious composites was developed. The material parameter calibration and constitutive laws adopted for the cementitious matrix and the lattice will first be introduced. The modeling processes for both lattices and lattice-reinforced composites are then presented, including geometry idealization, element selection, and contact definitions. Finally, the loading and boundary conditions consistent with the experimental configurations are summarized.

### 3.1. Material properties

The material properties for 3D-printed steel auxetic lattices were calibrated based on the tensile test in literature [85], where the same filament, 3D printer, and main printing settings were adopted to manufacture dog-bone specimens with different printing directions. The calibrated results compared to experimental measurements are shown in Fig. 1(b). The material properties corresponding to the flat printing configuration (i.e., 0° raster angle) were selected. This choice reflects the lattice printing strategy, which was designed without internal infill patterns and consisted of parallel walls aligned with the strut directions, as illustrated in Fig. 1(d). Consequently, the flat printing configuration was considered the most representative for the present study. Heterogeneity induced by inter-layer and intra-layer variations was idealized as homogeneous in this study, while these effects should be kept in mind for further improving model accuracy [86,87]. To characterize the failure process of steel, material ductile damage was considered. The adopted material properties for 3D-printed steel are summarized in Table 3. However, internal microporosity and anisotropy in the steel lattice struts can be introduced during debinding and sintering process: incomplete binder removal or differential shrinkage may lead to micro voids, while the sintering stage can result in non-uniform densification and residual stresses [88,89]. These factors might together influence mechanical performance of the lattice structures under compressive loading, leading to the brittle fracture compared to traditional cast steel [90]. Although the material parameters used in the simulations were

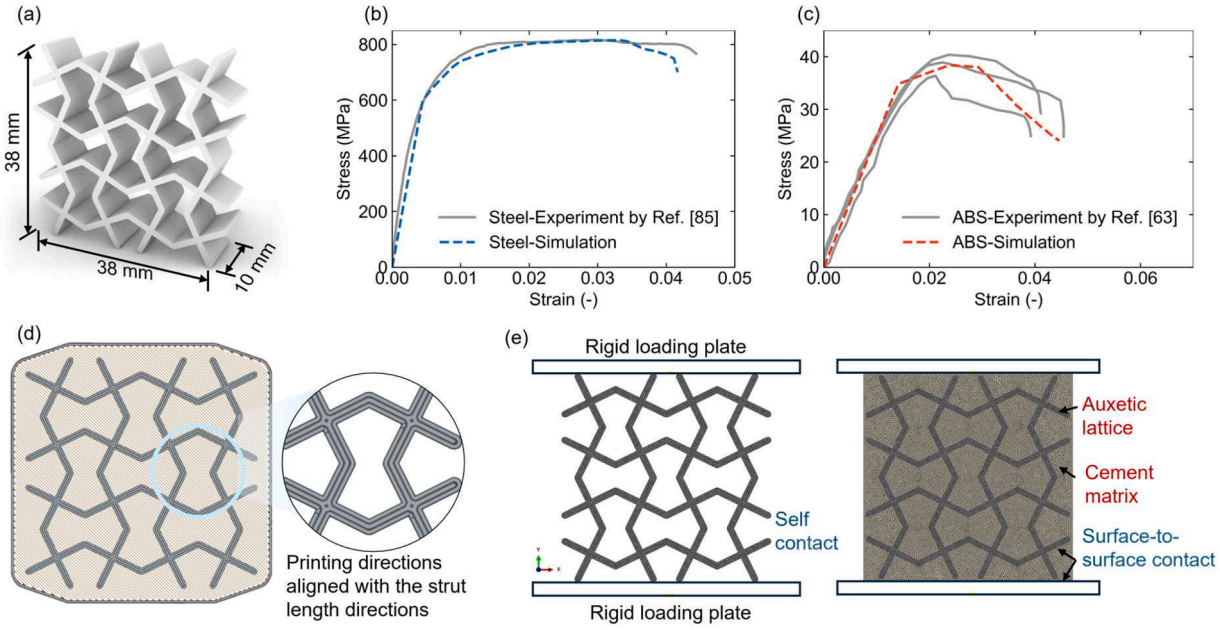


**Fig. 1.** Geometry, material calibration, and finite element modeling strategy for auxetic lattice and cementitious composite. (a) Geometry and overall dimensions of the rotating-square auxetic lattice structure. (b) Calibration of stress-strain relationships for 3D-printed steel against experimental results reported in [85]. (c) Calibration of stress-strain relationships for ABS against experimental results reported in [63] (note different stress scales for steel and ABS. (d) 3D printing directions for auxetic lattice, where the printing direction are aligned with the strut direction. (e) Finite element model of the auxetic lattice and auxetic cementitious composite under uniaxial compression.

**Table 3**
Material properties of 3D-printed steel and ABS.

| Parameters | Steel | ABS |
|---|---|---|
| Elastic modulus | 175 GPa | 1.9 GPa |
| Poisson's ratios | 0.44 | 0.20 |
| Yielding stress | 600 MPa | 35 MPa |
| Equivalent plastic strain at damage initiation | 0.03 | 0.02 |
| Fracture energy | 50 N/mm | 10 N/mm |
| Softening law | Linear | Linear |

calibrated through tensile testing of specimens produced using the same manufacturing procedure, it should be recognized that compressive response can be also sensitive to internal defects than tensile behavior.

In addition, the ABS material properties were also tested in the authors' previous study [63]. In this study, the material properties of ABS was also calibrated against the experimental measurement as shown in Fig. 1(c), and the calibrated parameters are also listed in Table 3. It can be seen that although the failure strains of both ABS and steel are similar, each reaching approximately 0.04, their post-peak behaviors differ significantly. ABS exhibits a clear softening branch before complete fracture, whereas steel fails more abruptly at a high stress level, releasing a larger amount of energy during final rupture. As for the cementitious matrix, the concrete damage plasticity model was used to simulate the matrix degradation process. The calibrated material properties can be found in the authors' previous studies, where both the compression and tension behaviors were tested and calibrated by using the same mixture proportions [63].

### 3.2. Model establishment

The finite element model was established using the commercial software ABAQUS/Explicit. Considering the planar nature of the tested specimens, both the matrix and the auxetic lattice geometry were modeled by two-dimensional plane elements, and a thickness of 10 mm was assigned while converting reaction force and displacement into stress and strain levels. In the simulation of the auxetic lattice, a self-contact algorithm was employed to characterize contact interactions between the auxetic lattice elements. For the composite simulations, the interface between the auxetic lattice and the cementitious matrix was modeled using surface-to-surface contact, where a hard contact in the normal direction and a friction coefficient of 1.0 in the tangential direction were adopted. This choice was based on the experimental observation that no apparent slip failure occurred between the steel auxetic reinforcement and the cement matrix, and this approach has also been employed by other studies simulating lattice-reinforced cementitious composites [91]. In Appendix B, a sensitivity analysis of the interfacial friction coefficient is presented to evaluate the influence of this modeling assumption on the predicted composite response. The results demonstrate that reduced friction coefficients lead to lower peak strength and diminished post-peak stress fluctuations, while friction coefficient of 1.0 can provide better agreement with experimental observations. Nevertheless, it should be noted that a more accurate characterization of the interfacial properties between 3D-printed lattices and cement matrices would provide deeper insights into the interaction mechanisms at smaller scales. In addition, two rigid plates were modeled to represent the loading plates, with a friction coefficient of 0.1 applied at the plate surface [59]. The model was meshed using CPS3 elements with an average mesh size of 0.4 mm. The overall model configuration is illustrated in Fig. 1(e).

## 4. Results and discussions

This section presents discussions to systematically reveal the mechanical behavior of 3D-printed auxetic lattice and their corresponding cementitious composites based on both experimental observations and numerical simulations. The mechanical responses of auxetic lattices are first discussed in terms of the load-bearing capacity, failure process and auxetic behaviors. Subsequently, the responses of composites reinforced by steel auxetic lattice are analyzed. Finally, the results of composites with soft polymer lattice was discussed, with particular attention given to the influence of stiffness contrast on confinement mechanisms and failure evolution. By comparing two composite systems, the role of material stiffness in activating confinement and modifying failure modes is clarified

### 4.1. Mechanical responses of 3D-printed auxetic lattice

Fig. 2a and Fig. 2b display the experimentally measured (solid lines with shaded regions) and numerically simulated (dashed lines) stress-strain responses of the steel and ABS auxetic lattices. The stress was obtained by dividing the reaction force by the nominal cross-sectional area, and the strain was calculated as the applied displacement normalized by the initial specimen height. The shaded regions represent the standard deviation from the mean response obtained from parallel experimental tests, reflecting the variability in mechanical performance. It can be seen that simulations show good agreement with experimental results for both materials, which validates the reliability of numerical model in predicting the mechanical responses of auxetic lattice structures. The fluctuations in the experimental results are mainly attributed to progressive local failures at lattice joints, which cause stiffness degradation and load redistribution. Since the stochastic nature of these local instabilities, differences might occur between simulation results and experimental measurements. In addition, the load-bearing capacity (defined as peak stress) of the steel-based auxetic lattices could reach 20 MPa, which was more than 10 times of these for ABS lattices. Despite the higher load bearing capacity, the 3D-printed steel auxetic lattices showed more pronounced load drops as indicated by the large standard deviation region. This behavior arises primarily from the complete fracture of load-carrying struts of the steel auxetic lattice. It can be seem from both experimental observations and numerical simulations that, once the global strain exceeds approximately 20% in Fig. 2e and Fig. 2f, the bottom struts were fully fractured. This complete fracture could interrupt the primary load-transfer paths and leads to load drops. In contrast, the ABS lattices showed smoother and more stable responses with gradual hardening and smaller fluctuations, which can be attributed to the less completely fractured struts and the more ductile damage evolution patterns of polymer-based materials. However, the relatively low stiffness and load-bearing capacity of the polymer material could limit its ability to fully constrain the cementitious matrix, which is further elaborated in the following sections

The different trends of stress-strain curves for steel and ABS auxetic lattice structures can also be explained from the failure process, as illustrated by the experimental and simulation results in Fig. 2(e-h). For the steel auxetic lattice, the simulation results showed stress concentrations at nearly all joint regions when the global strain reached approximately 5% (corresponding to a compression displacement of 2.0 mm). These concentrated stresses indicate the onset of localized yielding and potential crack initiation at the strut junctions. As loading progressed, the lattice underwent a gradual collapse characterized by joint failures starting from the regions adjacent to the loading plates (i.e., the top and bottom boundaries). This strut fracture of the steel auxetic lattices contributed to the pronounced load drops and stress fluctuations observed in the experimental stress–strain responses. When the strain reached 20%, most of the joints near the top and bottom regions were fully fractured, whereas the inner joints largely remained intact. As a result, the load previously carried by the fractured boundary struts was transferred to the adjacent intact joints and the inner unit cells. The simulation results also show that, following fracture of boundary struts, the inner region exhibited larger stress concentrations areas, and the location of stress concentration started to appear in strut rather than only at joints, which indicates a stress redistribution after the fracture of

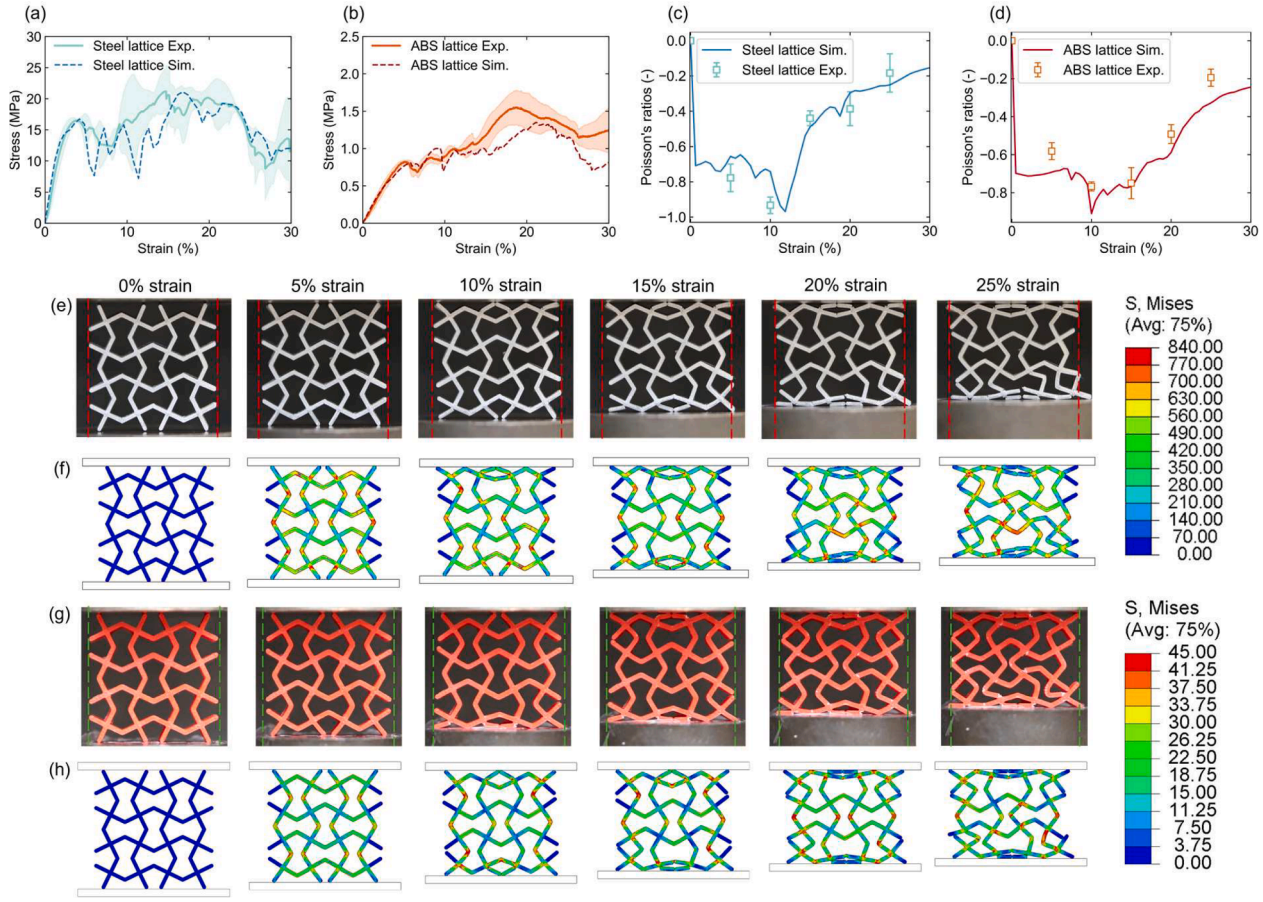


**Fig. 2.** Experimental and numerical responses of 3D-printed steel and ABS auxetic lattices under uniaxial compression. (a,b) Stress–strain curves of standalone auxetic lattices printed by steel and ABS respectively. Solid lines with shaded regions represent experimental averages and standard deviations from parallel tests, while dashed lines denote finite element simulations. (c,d) Evolution of inner-region Poisson's ratios for steel and ABS lattices, respectively. Symbols with error bars represent experimentally measurement, while solid lines denote numerical simulation results. (e) Experimental observed deformation and failure patterns of steel auxetic lattices at global strains of 0%, 5%, 10%, 15%, 20%, and 25%. (f) Simulated steel auxetic lattice with von Mises stress contours in units of MPa. (g) Experimental observed deformation and failure patterns of ABS auxetic lattices. (h) Simulated ABS auxetic lattice with von Mises stress contours in units of MPa.

boundary lattice struts. This explains the ability of the steel auxetic lattices to maintain some load carrying capacities after struts failure.

For the ABS auxetic lattice, the failure patterns from both experimental observations and simulation results are shown in Fig. 2(g) and Fig. 2(h), respectively. At the elastic stage (strain level of 5%), stress concentrations were observed in simulated stress distributions, while these concentrations were far less pronounced than those in the steel lattice. As indicated by the legends, the peak stress in the steel auxetic lattice reached approximately 840 MPa, whereas the ABS lattice was only about 45 MPa, which was 18 times lower. As the load continued to damage initiation stage (strain level 10%), the struts near the top and bottom boundaries began to show signs of damage, indicated by the whitening of joints due to localized plastic deformation. Simulation results also showed damage initiating at similar positions. This damage initiation process is similar with that of steel lattice, where joints close to boundaries would start fail first. Due to the gradual failure of the auxetic lattice, load drops can be witnessed while much milder compared to the steel auxetic lattice. At the damage propagation stage (strain level of 20%), damage extended to the internal joints, as indicated by the whitening areas. This damage propagation process differs with the behavior observed in the steel lattices. In steel lattice, no obvious cracks could be observed in interior regions and the later-stage failure evolution was predominantly concentrated near the boundaries, while ABS lattice showed more severe damage at the internal joints. This distinction is largely attributed to the earlier onset of softening of ABS compared with steel, as shown in Fig. 1(b) and Fig. 1(c).

The original sample width is indicated by the dashed lines in Fig. 2(e) and Fig. 2(g). It can be observed that the negative Poisson's ratio behavior is not visually obvious at low strain levels. This is mainly because the boundary friction between the lattices and loading plates may restrain lateral deformation near the edges, obscuring the auxetic response. As loading progressed, several fractured struts bent and extended outward beyond the original specimen boundary, resulting in an overall lateral expansion and a transition to a positive Poisson's ratio at the scale of the overall lattice structure. Since the failed joints were primarily concentrated near the sample boundaries, while the inner unit cells largely remained intact or less damaged, the evaluation of Poisson's ratio within the interior region of the lattice could provide a more suitable representation of the intrinsic auxetic behavior, which is independent of boundary-induced damage at the sample scale. In the numerical model, the displacements of the vertex points were extracted to compute the Poisson's ratio. However, experimentally determining the Poisson's ratio of lattice structures is different from simulation, as the central region of the lattice is largely hollow, making it difficult to place tracking points. Therefore, vertex points of the selected inner region were manually identified from the recorded images, and the relative lateral and longitudinal lengths were measured to calculate the Poisson's ratio. The details of the inner region and the selection of tracking points have been shown in Appendix C.

Fig. 2(c) and Fig. 2(d) present the comparison between simulated and experimentally evaluated Poisson's ratios in the inner region. Although some discrepancies are observed, likely due to manual

marking uncertainties and resolution limitations, the overall evolution trend agrees well with the numerical predictions. It can be observed from the figure that the interior regions exhibited clear auxetic behavior, even if no pronounced negative Poisson's ratio was observed at the overall lattice scale. Both lattice types initially contracted in the transverse direction, and their Poisson's ratios gradually approached zero as progressive damage occurred in the interior regions during loading. Notably, the steel auxetic lattice displayed more negative Poisson's ratios compared to the ABS auxetic lattice. This can be attributed to the reduced failure observed in the inner region of the steel auxetic lattice, whereas the ABS counterpart exhibited pronounced joint damage within the same region. Consequently, the steel auxetic lattice was able to better preserve the integrity of its internal auxetic architecture, thereby sustaining more negative Poisson's ratios at higher strain levels. Nevertheless, the persistence of negative Poisson's ratios in the inner region for both steel and ABS lattices suggests that the auxetic response of the internal lattice can still effectively confine the surrounding matrix, even when the overall Poisson's ratio of the composite approaches zero at the global scale due to the boundary effects.

In addition, although the observed difference between the inner-region Poisson's ratio and the global Poisson's ratio is closely related to scale-dependent boundary effects, for larger structural elements, such as walls or columns incorporating auxetic lattice reinforcement, the influence might become less significant as the interior volume becomes dominant. The macroscopic behavior may more closely reflect the auxetic behavior observed in the inner region of the lattice, provided that the auxetic architecture is sufficiently distributed throughout the structural domain. However, real structural components are subjected to more complex boundary conditions, including multi-axial stress states, load eccentricity, and construction-induced imperfections. These factors may modify the effective lateral deformation response at the structural scale. Therefore, further investigation through large-specimen testing or structural-scale numerical simulations is necessary to quantitatively assess the scale transition.

### 4.2. *Auxetic lattice-induced confinement and enhanced composite performance*

Fig. 3(a) compares the stress–strain responses of cementitious composites reinforced with steel auxetic lattices with the reference (unreinforced) sample. The reference mortar specimen exhibits a low peak strength of approximately 20 MPa and fails abruptly at a strain below 2%, which is aligned with the typical brittle fracture of plain cementitious materials. In contrast, the composites reinforced with steel auxetic lattices showed a peak strength over 80 MPa, nearly four times that of the reference mortar. Notably, this peak strength was still twice of the sum of the cement matrix (20 MPa) and reinforcement contributions (20 MPa), which suggests a strong composite action between the cement

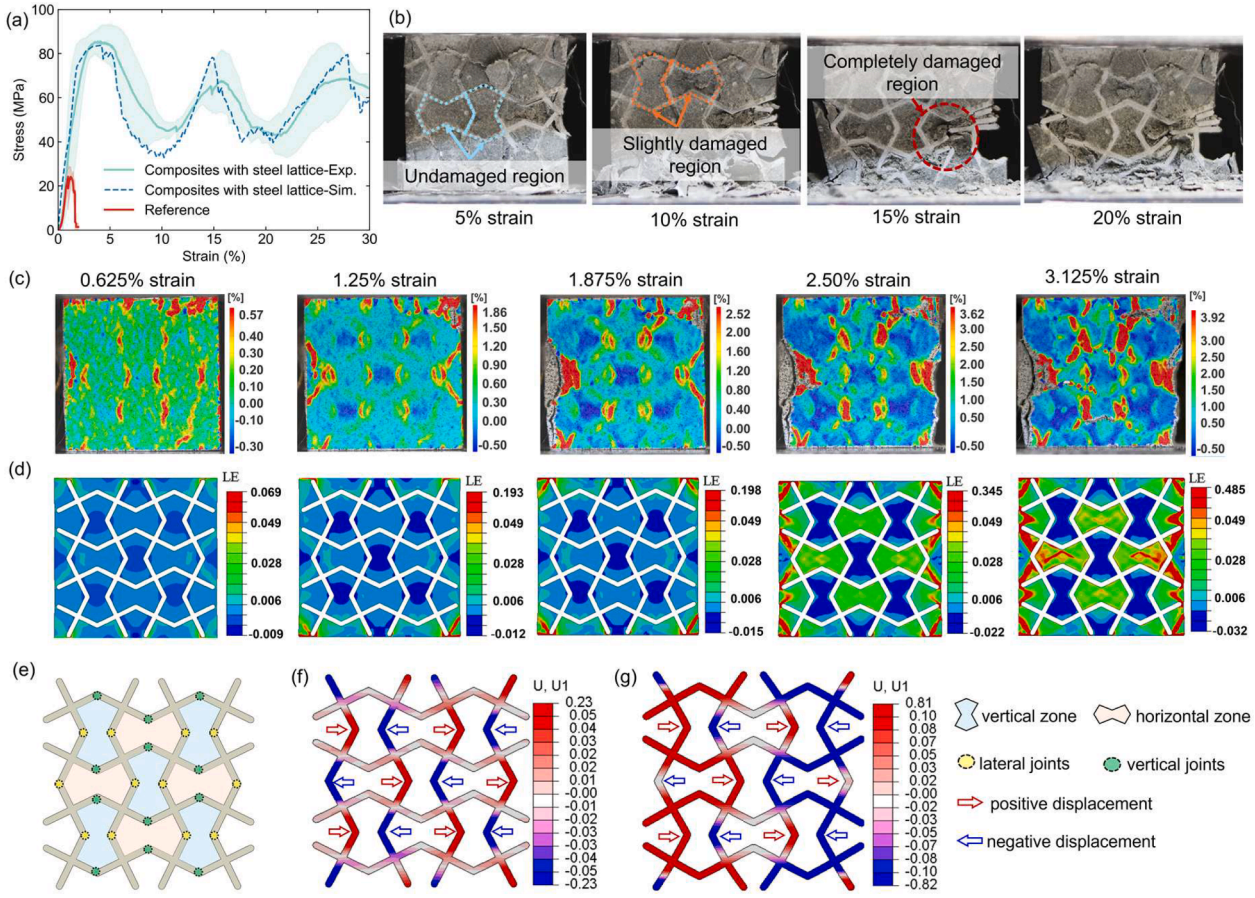


**Fig. 3.** Confinement mechanisms of cementitious composites reinforced with 3D-printed steel auxetic lattices. (a) Experimental (solid line for mean value and shaded region for standard deviation) and numerical (dashed line) stress–strain curves of composites with steel auxetic lattices under uniaxial compression, compared with the plain mortar reference (red). (b) Failure evolution of the composite at different global strain levels of 5%, 10%, 15%, and 20%. (c) DIC results showing major strain distributions for cementitious composites with steel auxetic lattices at different strain levels. Negative strain regions (blue) are inside the vertical lattice cells, indicating lateral confinement of the cement matrix. (d) Corresponding finite element simulations of principal strain distributions at the same strain levels. (e) Schematic illustration of the position of vertical and horizontal zones as well as vertical and lateral joints. (f,g) Horizontal displacement distributions at 3.125% global strain for (f) embedded lattice within the composite and (g) standalone lattice: red and blue colors denote positive and negative horizontal displacements, respectively.

matrix and the auxetic lattice that leads to synergistic enhancement of the load-bearing capacity. Moreover, the composite specimens showed multi-peak stress responses and sustained higher strain levels, indicating a gradual cracking and load redistribution within the composite system. Nevertheless, a relatively large scatter can be observed among the composite specimens (as indicated by the large shaded area), particularly in the post-peak range. This variability is mainly attributed to the brittle fracture characteristics of the 3D-printed steel lattice, as well as defects introduced during the debinding and sintering process, which can cause differences among specimens during the failure process. This can be also supported by the large variance observed for the standalone steel auxetic lattices in Fig. 2(a). Besides, the inherent variability in cementitious matrix during softening stage would also contribute to this variability. To minimize the influence of such variability, the averaged results among the three replicates would be used in the subsequent discussions.

As shown in Fig. 3(b), at a strain level of 5%, the cement matrix in the interior region remained largely intact under a stress of 80 MPa, with only minor surface spalling observed due to the absence of out-of-plane confinement. This intact region corresponds closely to the inner area exhibiting negative Poisson's ratios. This indicates that the lateral contraction of auxetic lattices can restrain the lateral expansion of the surrounding cement matrix under uniaxial compression. The kinematic restriction provides an effective confinement effect, which in turn contributes to the observed strength enhancement and delayed damage onset. At a strain level of 10%, the damage started to appear as deformations developed, and the exterior cementitious matrix was crushed which led to the stress drops. When the steel lattice subsequently fractured at a strain level of 15%, the stress–strain curve exhibited another sharp drop. Without the confinement from auxetic lattice, the cement matrix rapidly cracked and fragmented. With the progress of loading, the crushed matrix becomes compacted under compression, leading to a secondary rise in the stress level. However, it can be noticed that even under a strain of 20%, the cement matrix embedded in the central unit cell showed no noticeable cracking, which can be attributed to the lateral confinement from the intact lattice structure. In contrast, the matrix in fractured unit cells showed evident damage and cracking.

The simulated strain distributions are also compared with the digital image correlation in Fig. 3(c) and Fig. 3(d). It should be noted that the sprayed speckles on the specimen surface were partially lost due to the surface crumbling at large displacements, so only the correlation results up to the first peak load are presented. Both the experimental and numerical results consistently showed regions of negative in-plane principal strain inside the unit cells, which is caused by the confinement from auxetic reinforcement. This behavior confirms the steel auxetic lattice can effectively restrain the lateral expansion of the cementitious matrix under compression and thereby showing negative strain fields. With further increase of the compression, tensile strains along the inclined directions started to develop in the exterior regions where the auxetic lattice cannot provide sufficient confinement, as observed in both the experiments and the simulations. In the experimental testing, surface crumbling was also observed in these regions.

However, it can be observed from Fig. 3(d) that the negative strain regions were not uniformly distributed in the cementitious composites, but more concentrated within the vertical zones (as illustrated in Fig. 3 (e)) of the lattice and became increasingly more negative during the compression, whereas the cement matrix in horizontal zones gradually transitioned into positive strain. This phenomenon arises from the intrinsic deformation mechanism of the designed auxetic lattice. Fig. 3 (f) and Fig. 3(g) presents the horizontal displacement distributions for both embedded and standalone steel auxetic lattices at a strain level of 3.125%, respectively. It can be seen that in both cases the lateral joints (as highlighted in yellow shaded circles) exhibited a contraction tendency under compression, which imposed lateral confinement on the infilled cement matrix and resulted in the development of negative principal strain. At the same time, this lateral contraction of the vertical zones also caused the adjacent horizontal zones to expand outward, since both regions share common joints. Consequently, while the vertical zones enhance confinement of the cement matrix, the horizontal zones accommodate tensile deformation, leading to a different strain distribution between the vertical and horizontal zones. From a macroscopic perspective, this complementary deformation mechanism improves the overall mechanical performance of the composite system. The confinement in the vertical zones could mitigate crack initiation and propagation in the cement matrix, whereas expansion in the horizontal zones facilitates strain redistribution and energy dissipation, thereby reducing the likelihood of abrupt brittle failure. Furthermore, as shown in Fig. 3(g), the magnitude of horizontal displacement in the standalone auxetic lattice was greater than that in the embedded lattice within the composite. This is because the infilled matrix was effectively confined by the lattice's lateral contraction. Conversely, the presence of matrix can restrain the joint deformation of the lattice. This suggests that stiffness contrast between two constituent components might have an impact on the confinement effectiveness and the deformation pattern of the embedded lattice, which will be illustrated in the next Section.

### 4.3. Constituent stiffness contrast on auxetic cementitious composites

Fig. 4(a) compares the stress–strain responses of cementitious composites with ABS auxetic lattices against the reference cement mortar. It can be observed that the incorporation of the ABS auxetic lattice led to a reduction in the initial stiffness of the composite compared with the reference sample, primarily due to the lower elastic modulus of the polymer phase. Nevertheless, the peak compressive strength of the ABS lattice-reinforced composite remained comparable to that of the plain mortar, indicating that the auxetic architecture effectively compensated for the introduction of the softer phase. More importantly, the composite exhibited a gradual post-peak softening response, in contrast to the abrupt brittle fracture observed in the reference mortar. This enhanced post-peak behavior highlights the beneficial role of the embedded auxetic lattice in improving the deformability and toughness of the cementitious system.

In addition, the experimental results showed a gradual decrease after reaching the peak, while the simulation results showed a stress plateau. This difference was mainly attributed to the 2D assumption used in the present numerical model. The model with planar assumption would neglect out-of-plane failure modes, including delamination and thickness-direction instability. As shown in Fig. 4(b), because of the layered structure of 3D-printed ABS interlayer delamination of the ABS lattice was observed in the experiment. These characteristics along the thickness direction could influence stiffness degradation and damage evolution, while cannot be captured by the 2D model. Besides, the 2D model cannot explicitly consider the friction interactions between the lattice and cement matrix along the thickness direction. Although the auxetic behavior is designed to occur primarily in-plane, out-of-plane friction and confinement can influence the global stress redistribution and energy dissipation during compression. The absence of this mechanism may further affect the accuracy of post-peak predictions. Consequently, a fully three-dimensional model incorporating anisotropic properties would provide a more comprehensive representation of the failure process and should be considered.

Fig. 4(e) and Fig. 4(f) compares the experimentally measured strain fields obtained from digital image correlation with the simulated principal strain distributions for the composites reinforced with ABS auxetic lattices. At the initial stage where the strain level is below 1.25%, strain gradually localized along the vertical loading direction, primarily initiated from the lattice joints. With further loading, the initiation and propagation of vertical cracks within the cement matrix was observed, accompanied by pronounced strain accumulation along the left and right surfaces where the auxetic lattice could not provide full confinement. A similar strain localization pattern was also shown by finite element simulations, confirming that regions near the specimen's left

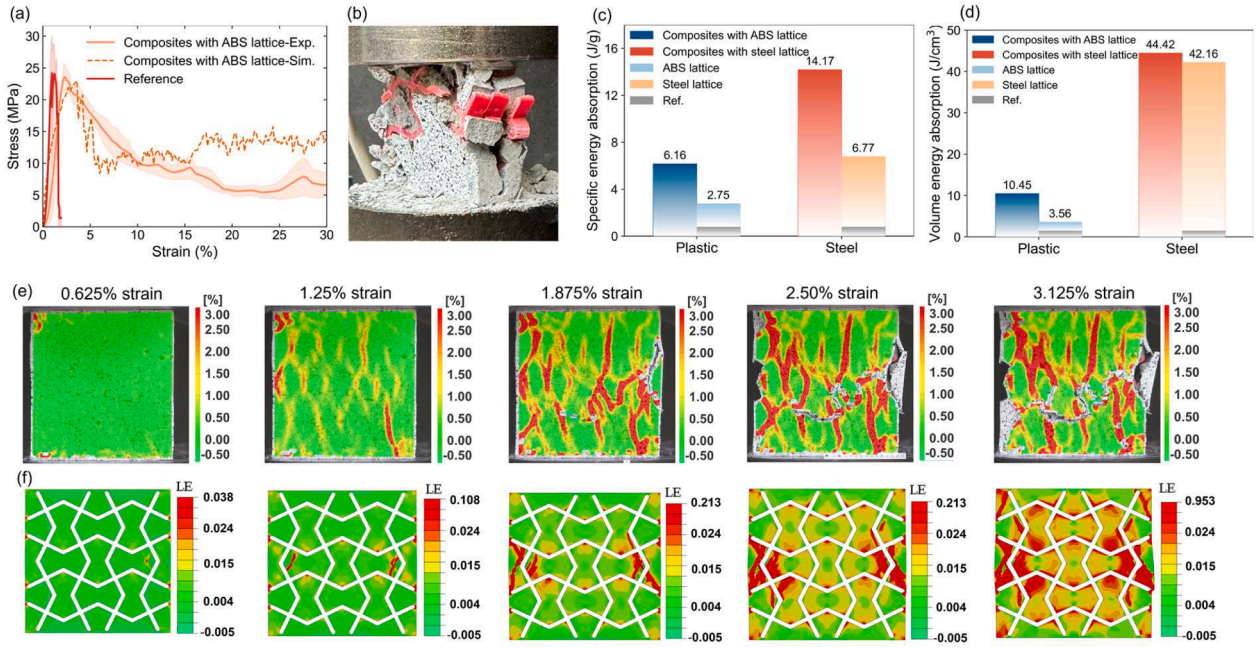


**Fig. 4.** Mechanical response, energy absorption, and strain evolution of cementitious composites reinforced with ABS auxetic lattices. (a) Experimental (solid line for mean value and shaded region for standard deviation) and numerical (dashed line) stress–strain curves of composites with ABS auxetic lattices under uniaxial compression, compared with the plain mortar reference (red). (b) Representative failure pattern of the ABS lattice-reinforced cementitious composite showing out-of-plane delamination. (c) Specific energy absorption (J/g) of cementitious composites, their individual lattice counterparts, and reference plain mortar up to a compressive strain of 30%. (d) Volumetric energy absorption (J/cm$^3$) of cementitious composites, their individual lattice counterparts, and reference plain mortar up to a compressive strain of 30%. (e) DIC results of the major strain distribution for cementitious composites with ABS auxetic lattices at different strain levels, where no pronounced negative lateral strain regions are observed, reflecting limited confinement from the low-stiffness lattice. (f) Corresponding finite element simulations of principal strain distributions.

and right boundaries experienced reduced reinforcement compared with the interior zones. Furthermore, unlike the composites reinforced with steel auxetic lattices, where distinct negative lateral strain fields were observed within the auxetic structure, the ABS lattice-reinforced composites exhibited no noticeable negative strain regions. This suggests that the ABS lattice provided less lateral constraint to the much stiffer cement matrix. Although the ABS lattice itself displayed auxetic deformation, its low stiffness limited its ability to translate this behavior into an effective confining stress on the surrounding matrix. Nevertheless, utilizing ABS auxetic lattice can still improve the post-peak ductility compared to reference mortar, suggesting that the auxetic effect of the ABS lattice contributed more to preventing brittle failure rather than to providing macroscopic confinement within the composite system.

Fig. 4(c) compares the specific energy absorption (i.e., total energy absorption divided by mass) of different lattice-reinforced cementitious composites, their individual lattice counterparts and reference plain mortar up to a compressive strain of 30%. In each bar group, the second column represents the summed energy absorption of the lattice reinforcement and the reference mortar, allowing a direct comparison with the composites. The results indicate that both ABS and steel auxetic lattices could enhance the energy absorption capacity of the cementitious composites compared with the reference matrix. The cementitious composite reinforced with the steel auxetic lattice exhibited the highest specific energy absorption, which was more than three times that of the polymer-lattice composite. However, it can be noted that the sum of the polymer lattice and reference mortar energy absorptions (2.75 J/g) was close to that of the composite with ABS auxetic lattice (6.16 J/g), suggesting a limited additive effect from the composite system. In contrast, the specific energy absorption of steel auxetic lattice reinforced composite (14.17 J/g) was significantly higher than the sum of steel lattice and reference mortar (6.77 J/g). This higher improvement ratio between the composite system and the sum of the two components indicates a strong synergy of the composite system, and the confinement from steel auxetic lattice can therefore improving the energy absorption capacity more efficiently. This result demonstrates that the higher stiffness contrast between the steel lattice and the cementitious matrix can lead to a higher additive effect in the composite system, and the matrix confinement from steel auxetic lattice attributed to the improved energy dissipation capacity. In addition, the volumetric energy absorption (energy per unit volume) is compared in Fig. 4(d) to provide a density-independent comparison. Due to the superior volumetric load-bearing capacity of steel compared to cement matrix, the volumetric energy absorption of standalone steel lattice is very close to that of the steel-reinforced composite. This indicates that, when evaluated on a volume basis, the energy dissipation capacity of the composite is largely influenced by the high intrinsic strength and stiffness of the steel phase. In contrast, the composites reinforced with ABS lattice exhibit substantially lower volumetric energy absorption, reflecting the limited contribution from the low-stiffness polymer phase. Nevertheless, it should be noted that although the steel phase showed better performances in improving energy absorption capacities, the choice of reinforcement material should be evaluated in the context of specific engineering requirements such as including weight, cost-effectiveness, and manufacturing complexity.

These findings highlight the critical role of constituent stiffness contrast in governing the mechanical properties of the auxetic cementitious composite systems. A higher reinforcement-to-matrix stiffness ratio ($E_{\text{lattice}}$ / $E_{\text{matrix}}$), as in the steel-reinforced system, enables more obvious constrain on the lateral deformation of the matrix, leading to enhanced load-bearing capacity and toughness. In contrast, a lower stiffness ratio reduces the confinement and the macroscopic auxetic effect, even when the lattice geometry itself remains auxetic. Although no evident confinement state was observed within the infilled matrix, the auxetic deformation of the polymer-based lattice altered the failure behavior of the composite from a brittle to a more ductile mode by promoting crack dispersion and the formation of multiple fine cracks

after reaching the peak load. Furthermore, the soft and flexible nature of the polymer-based lattices could still enable a smoother and more stable reduction of the load-carrying capacity compared to the reference mortar, avoiding large variations and brittle failure modes at high strain levels.

## 5. Representative volume element model analysis

The results presented above demonstrated that the stiffness contrast between the auxetic lattice and the cementitious matrix plays a critical role in governing the confinement effectiveness and overall mechanical response of auxetic cementitious composites. To further elucidate this mechanism at the mesoscale, a representative volume element (RVE) model was developed in this section. The basic concept of the RVE modeling approach is first introduced, including the periodic boundary conditions and determining homogenized mechanical properties. Subsequently, parametric studies were conducted by systematically varying the stiffness ratio between the lattice and the cement matrix, and the influence of stiffness ratio on stress distribution, confinement activation, and overall mechanical performance is discussed.

The geometry of the RVE model is illustrated in Appendix D, where a single unit cell was selected as the representative domain. As the RVE analysis was restricted to the elastic stage without considering interfacial damage, the lattice and matrix were modeled with shared nodes at their interface. In addition, The material properties of the auxetic lattice were then varied to achieve different stiffness ratios ($E_{\text{lattice}}$ / $E_{\text{matrix}}$) of 0.1, 1, 10, and 20. This range of stiffness ratios was selected to cover representative material classes relevant to practical lattice reinforcement in cementitious systems. The stiffness of the cement mortar is around 10 GPa. In comparison, soft polymers such as ABS typically exhibit an elastic modulus on the order of 1–3 GPa, resulting in a stiffness ratio of approximately 0.1. Hard polymers or materials with stiffness comparable to mortar correspond to a ratio close to 1. Light metals such as aluminum (stiffness between 60 and70 GPa) yield a stiffness ratio on the order of 10, while steel (stiffness between 190 and 210 GPa) corresponds to a ratio close to 20. Therefore, the selected stiffness ratios of 0.1, 1, 10, and 20 can reasonably represent soft polymer, hard polymer, aluminum, and steel-based lattice reinforcements, respectively.

During the modelling process, the edge nodes and vertex nodes were first sorted based on the coordinates, and the nodes on the opposite edges were then paired. After the node pairing was established, node-based constraint equations were generated to enforce the periodicity of displacements between each pair of corresponding nodes. The periodic boundary conditions (PBCs) were applied on the RVE model, where the control equations for uniaxial loading and shear loading are summarized in Table 4 and Table 5, respectively. The symbol $u$ represents the displacement components; the subscript $i$ represents the principal direction ($i = x, y$); the superscript represents the corresponding edge nodes or vertex nodes; RP1 and RP2 are reference points to control uniaxial loading on $x$ and $y$ directions; RP3 is the reference point to control the shear loading on the x-y plane. The displacement of each reference point, scaled by the RVE dimension, defines the corresponding macroscopic strain component applied to the representative volume element. For example, when a normal strain $\varepsilon_x$ is applied, a displacement $u_x^{RP1}$ equaling $\varepsilon_x \cdot L_x$ will be prescribed at RP1, where $L_x$ is the length of the RVE in the x-direction. The paired nodes on the left and right boundaries are then constrained so that their displacement difference in the x-direction equals $u_x^{RP1}$, Meanwhile, the displacement components

**Table 4**
Periodic boundary conditions for uniaxial loading.

| Edge nodes | Vertex nodes | |
|---|---|---|
| $u_i^{AB} - u_i^{DC} = u_i^{RP1}$ | $u_i^{A} - u_i^{D} = u_i^{RP1}$ | $u_i^{D} - u_i^{C} = u_i^{RP2}$ |
| $u_i^{BC} - u_i^{AD} = u_i^{RP2}$ | $u_i^{C} - u_i^{B} = u_i^{RP1}$ | $u_i^{B} - u_i^{A} = u_i^{RP2}$ |

**Table 5**
Periodic boundary conditions for shear loading.

| Edge nodes | Vertex nodes | |
|---|---|---|
| $u_x^{AB} - u_x^{DC} = u_x^{RP1}$ | $u_x^{A} - u_x^{D} = u_x^{RP1}$ | $u_y^{A} - u_y^{D} = u_y^{RP3}$ |
| $u_y^{AB} - u_y^{DC} = u_y^{RP3}$ | $u_x^{D} - u_x^{C} = u_x^{RP3}$ | $u_y^{D} - u_y^{C} = u_y^{RP2}$ |
| $u_x^{BC} - u_x^{AD} = u_x^{RP3}$ | $u_x^{C} - u_x^{B} = u_x^{RP1}$ | $u_y^{C} - u_y^{B} = u_y^{RP3}$ |
| $u_y^{BC} - u_y^{AD} = u_y^{RP2}$ | $u_x^{B} - u_x^{A} = u_x^{RP3}$ | $u_y^{B} - u_y^{A} = u_y^{RP2}$ |

associated with the other deformation modes at RP2 and RP3 are set to zero. In this way, the imposed deformation corresponds to a pure uniaxial strain of $\varepsilon_x$ along x-direction. Once the boundary conditions were prescribed, the homogenized constitutive response of the composite was obtained from the RVE simulations by computing the volume-averaged stress and strain. Specifically, the stress was calculated as the reaction force divided by the representative cross-sectional area (i.e., specimen length multiplied by the prescribed thickness of 10 mm), while the strain was determined as the applied displacement normalized by the corresponding specimen length.

After obtaining the homogenized Young's moduli, Poisson's ratios, and shear moduli along the principal directions, the anisotropic Young's modulus projected on an arbitrary direction can be expressed as

$$\frac{1}{E(\boldsymbol{n})} = S_{ijkl} n_i n_j n_k n_l, \tag{1}$$

where $S_{ijkl}$ is the compliance tensor and $\boldsymbol{n}$ is the directional tensor. Based on this formulation, the elastic surface can be constructed to visualize the directional dependence of the effective stiffness.

In addition to the Young's modulus, the directional Poisson's ratio can also be evaluated. For a given loading direction $\boldsymbol{n}$ and a transverse observation direction $\boldsymbol{d}$ (orthogonal to $\boldsymbol{n}$), the directional Poisson's ratio is defined as

$$\nu(\boldsymbol{n}, \boldsymbol{d}) = -\frac{\varepsilon_{dd}}{\varepsilon_{nn}}, \tag{2}$$

where $\varepsilon_{nn} = \varepsilon_{ij} n_i n_j$ represents the normal strain in the loading direction; $\varepsilon_{dd} = \varepsilon_{ij} d_i d_j$ represents the lateral strain in the transverse direction; $\varepsilon_{ij} = S_{ijkl} n_k n_l$ is the strain tensor obtained from the generalized Hooke's law $\varepsilon_{ij} = S_{ijkl}\sigma_{kl}$. Therefore, the directional Poisson's ratio can be further expressed as the following equation. By varying the loading direction $\boldsymbol{n}$ in the x-y plane and choosing $\boldsymbol{d}$ as the orthogonal observing direction within the plane, the directional Poisson's ratio distribution can be obtained as

$$\nu(\boldsymbol{n}, \boldsymbol{d}) = -\frac{S_{ijkl} d_i d_j n_k n_l}{S_{ijkl} n_i n_j n_k n_l}. \tag{3}$$

Fig. 5(a) and Fig. 5(b) illustrates the equivalent elastic modulus surfaces and Poisson's ratios for varying lattice-to-matrix stiffness ratios, respectively. When the lattice is softer than the matrix, the equivalent elastic modulus surface appeared nearly circular but still displayed slight convexity along the principal axes. The corresponding Poisson's ratios along these directions remained above 0.2 (the Poisson's ratio of the matrix), indicating that the lattice provided only limited confinement effect in the composite system. For the case where the lattice and matrix had comparable stiffness, the modulus surface remained almost isotropic, and the Poisson's ratios were uniformly distributed, reflecting homogeneous mechanical properties in the elastic range. As the auxetic lattice stiffness increased, distinct anisotropic features emerged. At a stiffness ratio of 10, the equivalent elastic modulus surface became convex again along the principal axes, while the associated Poisson's ratios decreased toward approximately 0.2, showing the onset of confinement effects. When the stiffness ratio further increased to 20, which is representative of steel-based auxetic lattices, the anisotropy was more pronounced. The elastic modulus distribution developed distinct lobes aligned with the principal directions which were also the

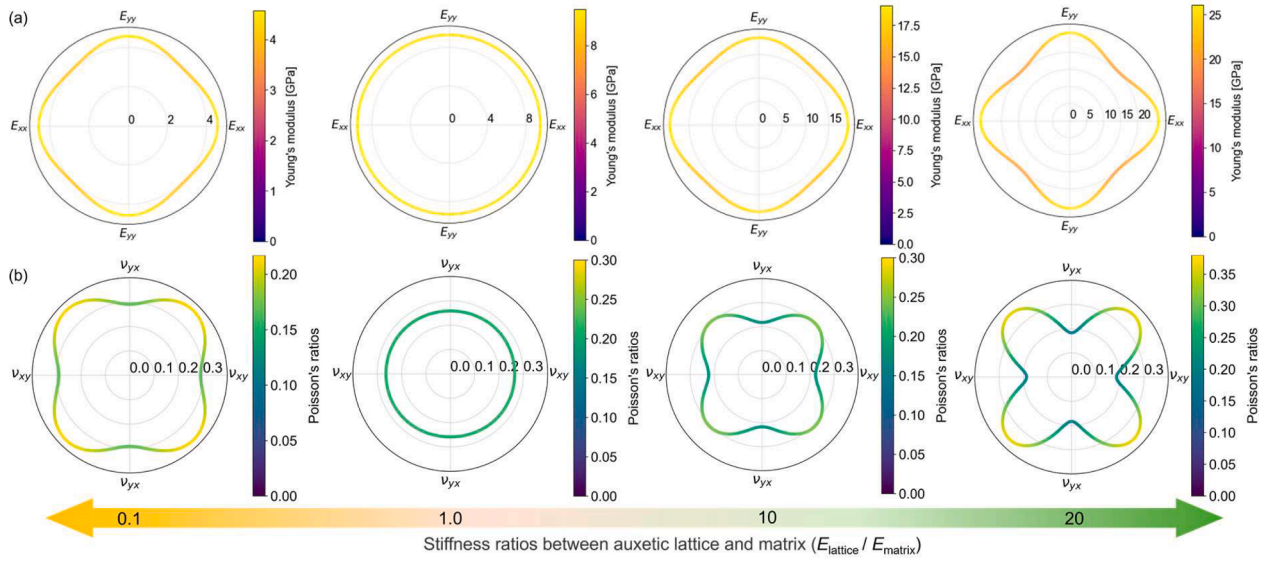


**Fig. 5.** Equivalent elastic properties of auxetic cementitious composites predicted by RVE analysis at lattice-matrix stiffness ratios of 0.1, 1.0, 10, and 20. (a) Equivalent elastic modulus surfaces. (b) Directional Poisson's ratios.

lattice's symmetry axes. The Poisson's ratios exhibited strong directional dependence, where values dropped below 0.2 along the principal axes but increased significantly along diagonal directions (e.g., 45° away from the principal axes). This suggests that the designed auxetic lattice could only provide strong confinement along specific directions because of its two-dimensional nature. Overall, these results highlight the critical role of stiffness mismatch in controlling both the effective elastic properties and the confinement efficiency of lattice-reinforced composites. While low-stiffness lattices contribute little to confinement, stiffer lattices amplify anisotropy and directional confinement, thereby improving the composite action of the system.

In addition, it can be noticed that, for both low and high lattice-to-matrix stiffness ratios, the slight convexity of the elastic modulus surfaces along the principal axes (i.e., $E_{xx}$ and $E_{yy}$) could be consistently observed. This feature is primarily attributed to the geometric symmetry of the unit cell, in which the principal directions provide the most direct and continuous load-transfer paths. When the lattice is relatively soft, the matrix dominates the load-bearing response, and matrix's infill pattern (also symmetrical along the principal axes) makes the RVE model show stronger stiffness along the principal directions. Conversely, when the lattice is much stiffer than the matrix, the stiff lattice struts aligned with the principal directions govern the deformation, again producing enhanced stiffness along these directions. However, the lattice was less effective in resisting shear or off-axis loads compared to the bulk matrix, which results in relatively lower stiffness along diagonal directions. This explains why the convexity along the principal axes persists regardless of the stiffness ratio, but significant anisotropy could be observed as the lattice stiffness increases.

The lateral principal strain distributions under vertical compression are presented in Fig. 6 for different stiffness ratios between the auxetic lattice and the cementitious matrix. When the stiffness of the auxetic lattice is lower than or comparable to that of the cement matrix (i.e., $E_{lattice}$ / $E_{matrix}$ is lower than 1), limited negative lateral strains can be observed within the composite, indicating that the auxetic deformation of the lattice con provide minimal confinement to the surrounding matrix. In these cases, the softer or equally stiff lattice deforms together with the matrix, and the lateral contraction characteristic of the auxetic structure is largely suppressed by the surrounded cementitious matrix. Nevertheless, some localized confinement can still be observed near the lattice joint regions where the lattice exhibits higher geometric stiffness. As the stiffness ratio increases (i.e., $E_{lattice}$ / $E_{matrix}$ = 10 and 20), more pronounced negative lateral strains develop near the lattice ribs, demonstrating a stronger auxetic response and effective lateral confinement of the matrix. This behavior is primarily attributed to the increased stiffness contrast between the lattice and the matrix, which enables more efficient stress transfer and deformation control within the composite. These results illustrate that the confinement effect in auxetic cementitious composites is highly dependent on the relative stiffness of the two components, where a sufficiently high stiffness contrast is required to fully activate the auxetic deformation and maximize the beneficial confinement of the cementitious matrix, while low stiffness contrast (or low material stiffness of the auxetic lattice) can only lead to some localized confinement near the joints rather than global matrix confinement within the composite systems.

Based on the RVE results, it is possible to provide a preliminary design recommendations of the stiffness contrast effect. When the stiffness ratio is smaller than 1, the auxetic can hardly provide sufficient lateral confinement, and the mechanical response remains largely

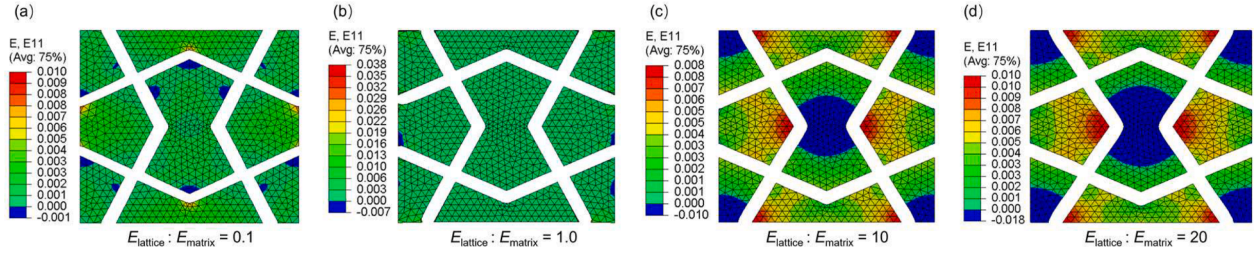


**Fig. 6.** Lateral principal strain distributions under vertical load for RVE with different lattice-to-matrix stiffness ratios. (a) Strain distributions at a stiffness ratio of 0.1. (b) Strain distributions at a stiffness ratio of 1.0. (c) Strain distributions at a stiffness ratio of 10. (d) Strain distributions at a stiffness ratio of 20.

matrix-dominated. As the stiffness ratio increases to approximately 10, a pronounced confinement effect becomes evident, characterized by noticeable reduced Poisson's ratios along the principle directions and restrained strain distributions within the matrix. Further increasing the stiffness ratio to 20 continues to improve the confinement efficiency, although the incremental gain becomes less significant compared with the transition from 1 to 10. Therefore, from a practical design perspective, a stiffness ratio on the order of 10 or higher may be considered a reasonable lower bound for activating a meaningful confinement effect in cementitious composites. It should be noted, however, that material selection in real engineering applications must also account for additional considerations such as cost-effectiveness, manufacturability, and durability, rather than relying solely on stiffness contrast.

## 6. Conclusions

This study presents a combined experimental and numerical investigation on auxetic cementitious composites with 3D-printed auxetic lattices by materials of distinct stiffnesses. The mechanical performances of the composites were examined through uniaxial compression tests, accompanied by digital image correlation and finite element simulations to capture confinement state as provided by the auxetic lattice structures. Furthermore, representative volume element analyses incorporating periodic boundary conditions were performed to derive the homogenized elastic properties of the orthotropic composite system and to clarify the effect of constituent stiffness contrast.

The results demonstrate that stiffness contrast between the auxetic lattice and the cementitious matrix is the governing parameter controlling confinement effectiveness, damage evolution, and overall mechanical performance. When reinforced with steel auxetic lattices, the composites exhibited a remarkable enhancement in load-bearing capacity and energy absorption. The peak strength increased by approximately 300% relative to the plain matrix, and the specific energy absorption of the composite was 90% greater than the combined energy absorption of the standalone steel lattice and the mortar, indicating strong composite action and active confinement induced by the auxetic lattice structure.

In contrast, cementitious composites reinforced with ABS auxetic lattices primarily showed improvement in deformability rather than strength. Although the peak strength and energy absorption were lower than those of the steel-lattice composites, the polymer lattice effectively mitigated the brittle failure mode of the cement matrix and promoted a smoother post-peak response. The relatively low stiffness contrast between ABS and the mortar limited the activation of confinement, resulting in a weaker synergistic enhancement. These comparisons clearly indicate that the confinement mechanism is strongly dependent on the stiffness ratio between lattice and matrix phases.

The combined use of DIC measurements and finite element simulations provided consistent evidence of confinement- within the composites. Steel lattices generated pronounced lateral constrains in interior regions, leading to the activation of confinement from auxetic lattice, whereas the ABS lattices exhibited more dispersed cracking patterns without significant confinement. Furthermore, the RVE analysis revealed that increasing stiffness contrast enhances effective elastic moduli and promotes more distinct orthotropic behavior. Parametric studies suggest that a stiffness ratio equal or higher than 10 can be considered as the lower bound to activate meaningful confinement and produce substantial macroscopic performance gains.

By combining experimental test, numerical simulations, and meso-scale RVE analyses, this work establishes a clear mechanistic link between stiffness contrast, auxetic deformation, and confinement effectiveness in lattice-reinforced cementitious composites. The findings provide practical guidance for material selection and structural design. However, several aspects still require further investigation. The current work primarily focused on two-dimensional steel auxetic lattice, while 3D-printed steel lattice structures in three-dimensional cases should be further investigated. In addition, interface bonding control between the lattices and the cementitious matrix, as well as the effects of lattice geometry, scale, and material heterogeneity, should be further explored to optimize the design of such composites. Finally, further research examining the behavior of auxetic cementitious composites with 3D-printed steel lattice under various loading conditions, including tension, bending, and fatigue, is necessary to establish a more complete understanding of their performance and failure mechanisms.

## CRediT authorship contribution statement

**Zhaozheng Meng:** Writing – review & editing, Writing – original draft, Visualization, Validation, Methodology, Investigation, Formal analysis, Data curation, Conceptualization. **Yading Xu:** Writing – review & editing, Validation, Methodology, Investigation, Formal analysis, Conceptualization. **Wen Zhou:** Writing – review & editing, Visualization, Methodology, Investigation, Formal analysis. **Rowin J.M. Bol:** Writing – review & editing, Validation, Software, Methodology, Investigation. **Jinbao Xie:** Writing – review & editing, Methodology, Formal analysis, Data curation. **Branko Šavija:** Writing – review & editing, Supervision, Resources, Project administration, Methodology, Funding acquisition, Formal analysis, Conceptualization.

## Declaration of competing interest

The authors declare that they have no known competing financial interests or personal relationships that could have appeared to influence the work reported in this paper.

## Acknowledgements

Zhaozheng Meng, Yading Xu, Wen Zhou, Rowin J.M. Bol and Branko Šavija acknowledge the financial support from the European Research Council (ERC) within the framework of the ERC Starting Grant Project "Auxetic Cementitious Composites by 3D printing (ACC-3D)", Grant Agreement Number 101041342. Views and opinions expressed are however those of the author(s) only and do not necessarily reflect those of the European Union or the European Research Council. Neither the European Union nor the granting authority can be held responsible for them. Jinbao Xie would like to acknowledge the funding supported by China Scholarship Council (CSC) under the grant CSC No. 202006260045.

## Appendix A. Unit cell design parameters

Fig. A.1 illustrates the geometric configuration of the auxetic unit cell adopted in this study. The overall dimension of the unit cell is 19 mm. The joint-to-joint strut length of the unit cell is 5 mm, and the internal angle is designed as 128° The strut width is set as 1.2 mm, which was determined based on the manufacturability constraints of the fused filament fabrication process while maintaining sufficient stiffness during mechanical loading.

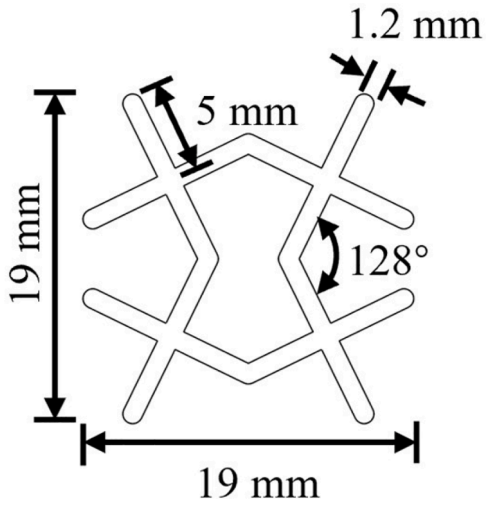


**Fig. A.1.** Geometric configuration of the unit cell for auxetic lattice adopted in this study.

## Appendix B. Sensitivity analysis of interfacial friction coefficients

To evaluate the influence of the interfacial bonding between the auxetic lattice and the cementitious matrix, a sensitivity analysis was conducted by varying the friction coefficient adopted in the surface-to-surface contact. In the numerical model presented in Section 3.2, a friction coefficient of $\mu = 1.0$ was selected, while additional simulations were performed here with friction coefficients of $\mu = 0.1$, 0.3, 0.5, and 0.7. The corresponding stress–strain responses are shown in Fig. B.1. It can be observed that when the friction coefficient is low ($\mu = 0.1$ and 0.3), the predicted peak strength decreases compared to the experimental average curve. Furthermore, the post-peak stress fluctuations observed experimentally are also reduced. This behavior indicates that insufficient interfacial friction might lead to relative sliding between the lattice and the matrix, thereby weakening the confinement effect and limiting effective stress transfer. As the friction coefficient increases, both the peak strength and the post-peak response progressively approach the experimental results. For friction coefficients larger than 0.5, the simulated curves show good agreement with the experimental average. When the friction coefficient further increased 2.0, the load response showed little difference compared to that with a coefficient of 1.0. These findings suggest that a sufficiently strong interface is necessary to accurately simulate the auxetic-induced confinement mechanism in the composite system.

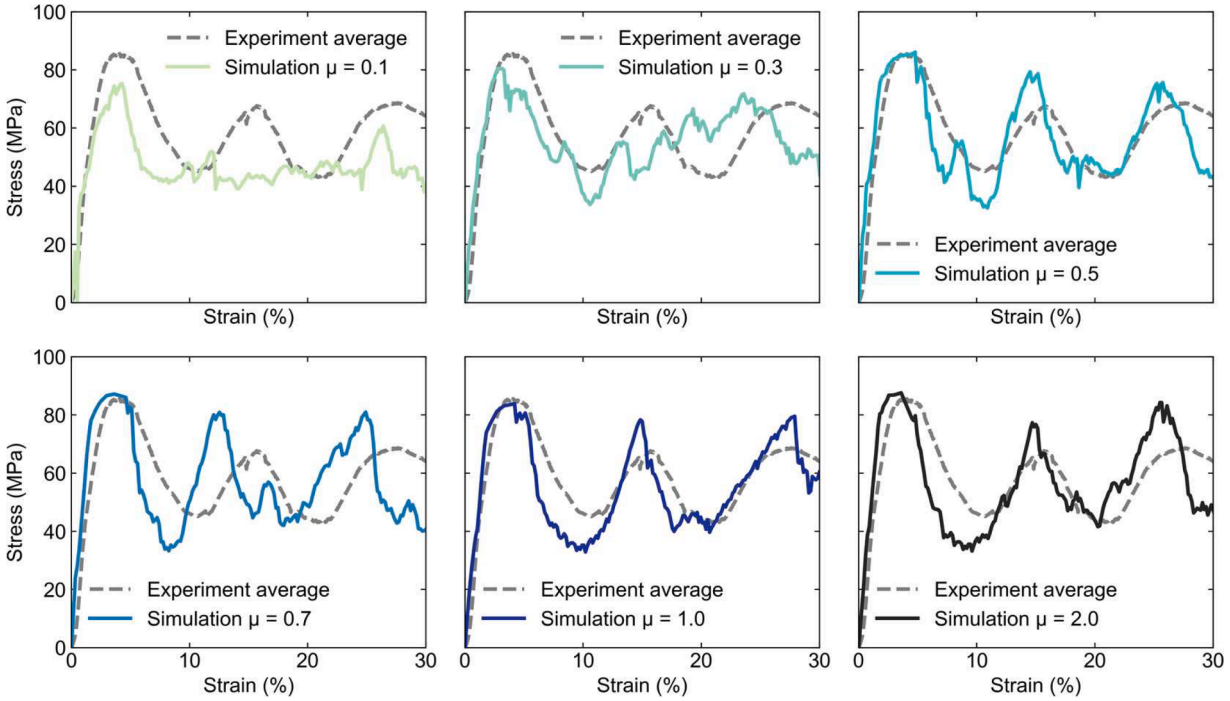


**Fig. B.1.** Influence of interfacial friction coefficient on the simulation results of steel auxetic reinforced cementitious composites, where the friction coefficient was varied between 0.1 and 2.0.

## Appendix C. Definition of inner region and Poisson's ratio evaluation

To characterize the intrinsic auxetic response of the lattice independent of boundary-induced damage, an interior region was defined for Poisson's ratio evaluation, as illustrated in Fig. C.1. The selected region corresponds to a square area located at the geometric center of the lattice structure with a side length of 19 mm. This region was chosen to minimize the influence of boundary effects, such as premature joint fracture near the loading plates and friction-induced constraints, which may obscure the auxetic deformation at the specimen scale.

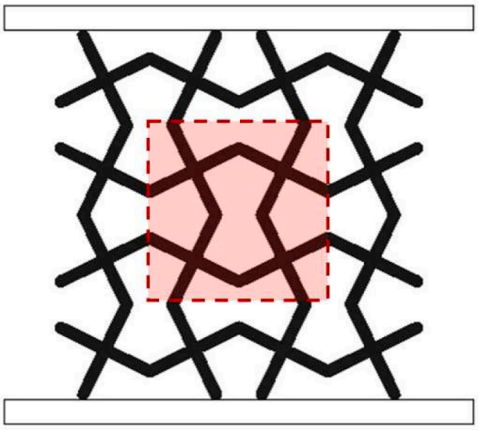

**Fig. C.1.** Schematic illustration of the inner region (red dashed box) for Poisson's ratio evaluation.

In experiments, the Poisson's ratio was evaluated based on relative distances between the four vertex points of the selected interior region. As shown in Fig. C.2, the longitudinal and transverse distances between the corresponding vertex points were tracked during loading. The engineering strain in the loading direction was calculated from the vertical displacement difference divided by the initial vertical distance, while the transverse strain was determined from the horizontal displacement difference normalized by the initial horizontal distance. The Poisson's ratio was then obtained as the negative ratio between the transverse strain and the longitudinal strain. It should be noted that as strut fracture and large deformation occur, the geometric integrity of the interior region may gradually deteriorate, making the identification of the original vertex points less precise. This geometric evolution may introduce additional uncertainty in the displacement measurement and consequently lead to errors in the calculated Poisson's ratio.

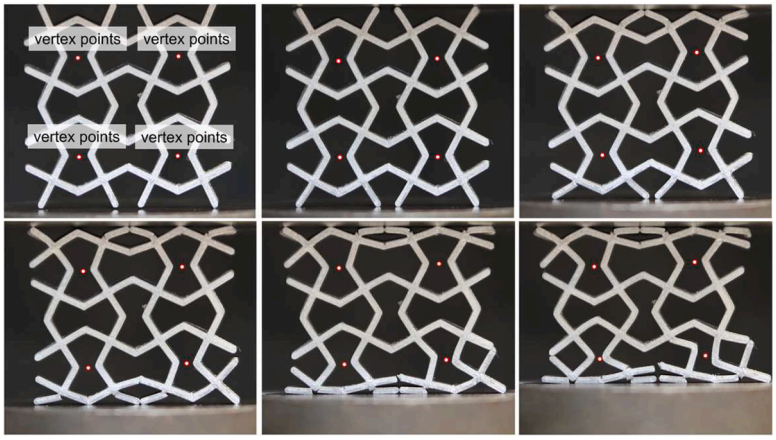


**Fig. C.2.** Vertex points of the interior region for experimentally determining Poisson's ratios.

In numerical simulations, the same vertex points defining the interior region were identified in the finite element model. Their displacement histories were directly extracted from the simulation output and used to compute the Poisson's ratio, which ensure the comparability between experimental measurements and numerical simulations.

## Appendix D. RVE model setup

The representative volume element (RVE) model adopted in this study is illustrated in Fig. D.1. A single periodic unit cell was selected as the representative domain. Both the auxetic lattice and the cementitious matrix were modeled explicitly within the same geometric domain, and perfect bonding between the two phases was assumed by using shared nodes at the interface. The mesh consisted of two-dimensional plane stress elements, consistent with the modeling framework described in Section 3.

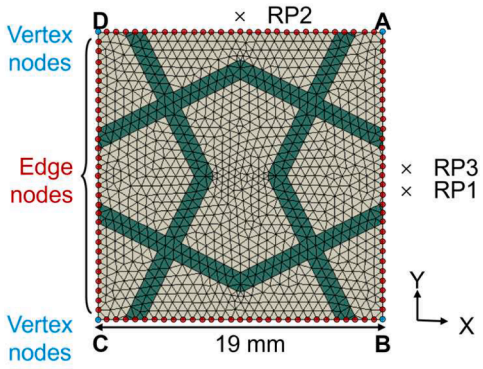


**Fig. D.1.** RVE model setup illustrating boundary nodes for the implementation of periodic boundary conditions.

To ensure periodicity of deformation, periodic boundary conditions (PBCs) were applied to the RVE boundaries. As shown in Fig. D.1, the boundary nodes were categorized into vertex nodes (located at the four corners) and edge nodes (located along the four edges excluding the corners). Prior to imposing the constraints, nodes along opposite edges were first sorted according to their coordinates and paired accordingly to guarantee one-to-one correspondence. This pairing ensures that the displacement field remains compatible across opposite boundaries.

The periodic boundary conditions were implemented by enforcing displacement constraints between each pair of corresponding nodes on opposite edges. Specifically, the displacement difference between paired nodes was constrained to be equal to the macroscopic strain components multiplied by the RVE dimensions. Reference points were introduced to prescribe the macroscopic normal and shear strain components, and their displacements were linked to the boundary nodes through constraint equations.

## Data availability

Data will be made available on request.

## References

[1] Wu Z, Pan H, Huang P, Tang J, She W. Biomimetic mechanical robust cement-resin composites with machine learning-assisted gradient hierarchical structures. Adv Mater 2024;36(35).
[2] Krystek M, Pakulski D, Patroniak V, Górski M, Szojda L, Ciesielski A, et al. High-performance graphene-based cementitious composites. Adv Sci 2019;6(9).
[3] Yu K, Li L, Yu J, Wang Y, Ye J, Xu Q. Direct tensile properties of engineered cementitious composites: a review. Constr Build Mater 2018;165:346–62.
[4] Yang J, Paz CM, Estefen SF, Fu G, Lourenço MI. Collapse pressure of sandwich pipes with strain-hardening cementitious composite - part 1: experiments and parametric study. Thin-Walled Struct 2020:148.
[5] Juenger MCG, Siddique R. Recent advances in understanding the role of supplementary cementitious materials in concrete. Cem Concr Res 2015;78:71–80.
[6] Tong LY, Liu QF, Gruyaert E, Alderete NM, Xiong QX, De Belie N. Experimental and numerical study on carbonation of blast-furnace slag concrete considering the microstructural evolution. Cem Concr Res 2026:200.
[7] Shi M, Han J, Zhang D. Elucidate the influence of polymers on the energy storage characteristics of cementitious composites. Cement Concrete Comp; 2026. p. 165.
[8] Martuscelli CC, dos Santos JC, Oliveira PR, Panzera TH, Aguilar MTP, Garcia CT. Polymer-cementitious composites containing recycled rubber particles. Constr Build Mater 2018;170:446–54.
[9] Sahmaran M, Yildirim G, Erdem TK. Self-healing capability of cementitious composites incorporating different supplementary cementitious materials. Cem Concr Comp 2013;35(1):89–101.
[10] Xie J, He S, Xu Y, Meng Z, Zhou W, Schlangen E, et al. Enhanced elastomer-like auxetic cementitious materials through strain-hardening cementitious composites (SHCC) with extended softening properties. Cement Concrete Comp; 2025. p. 161.
[11] Gupta S, Esmaeeli HS, Moini R. Tough and ductile architected nacre-like cementitious composites. Adv Funct Mater 2024;34(39).
[12] Asad M, Win N, Zahra T, Thambiratnam DP, Chan THT, Zhuge Y. Enhanced energy absorption of auxetic cementitious composites with polyurethane foam layers for building protection application. J Build Eng 2023;78.
[13] Jin P, Kohestanian M, Hasany M, Akhiani AR, Su YL, Mehrali M. Multifunctional cement-based composite with advanced self-sensing, electrothermal, and electrochemical properties. Adv Funct Mater 2025;35(13).
[14] Prihar A, Gupta S, Esmaeeli HS, Moini R. Tough double-bouligand architected concrete enabled by robotic additive manufacturing. Nat Commun 2024;15(1).
[15] Wang F, Du Y, Jiao D, Zhang J, Zhang Y, Liu Z, et al. Wood-inspired cement with high strength and multifunctionality. Adv Sci 2021;8(3).
[16] Imagawa K, Ohno M, Koga Y, Ishida T. Cement-based mechanical metamaterials with spiral resonators for vibration control, 163. Cement Concrete Comp; 2025.
[17] Chen M, Yao X, Zhu L, Yin M, Xiong Y, Hu N. Geometric design and performance of single and dual-printed lattice-reinforced cementitious composite. Cement Concrete Comp; 2023. p. 143.
[18] Salazar B, Aghdasi P, Williams ID, Ostertag CP, Taylor HK. Polymer lattice-reinforcement for enhancing ductility of concrete. Mater Des 2020;196.
[19] Zahra T. Behaviour of 3D printed re-entrant chiral auxetic (RCA) geometries under in-plane and out-of-plane loadings. Smart Mater Struct 2021;30(11).
[20] Cheng X, Zhang Y, Ren X, Han D, Jiang W, Zhang XG, et al. Design and mechanical characteristics of auxetic metamaterial with tunable stiffness. Int J Mech Sci 2022:223.
[21] Wang LQ, Tong JZ, Pan ZS, Evans KE, Shen JJ. Poisson's ratio control in auxetic metamaterials under large tensile strains. Int J Mech Sci 2025;304.
[22] Han D, Li P, Li P, Li LI, Bai C, Fan H, et al. Utilizing partially-curved-beam to improve stress response and energy absorption performance of auxetic lattice metamaterials. Thin-Walled Struct 2025:217.
[23] Han D, Ren X, Zhang Y, Zhang XY, Zhang XG, Luo C, et al. Lightweight auxetic metamaterials: design and characteristic study. Compos Struct 2022:293.
[24] Chen Z, Wu X, Xie YM, Wang Z, Zhou S. *Re*-entrant auxetic lattices with enhanced stiffness: a numerical study. Int J Mech Sci 2020;178.
[25] Choudhry NK, Panda B, Kumar S. Enhanced energy absorption performance of 3D printed 2D auxetic lattices. Thin-Walled Struct 2023;186.
[26] Meng Z, Xu Y, Xie J, Zhou W, Bol RJM, Liu Q-F, et al. Unraveling the reinforcing mechanisms for cementitious composites with 3D printed multidirectional auxetic lattices using X-ray computed tomography. Mater Des 2024:246.
[27] Vitalis T, Gross A, Tzortzinis G, Schagen B, Gerasimidis S. Enhancing mortar composite matrices with three-dimensional auxetic truss lattice materials for reinforced concrete structures. Constr Build Mater 2024:457.
[28] Momoh EO, Jayasinghe A, Hajsadeghi M, Vinai R, Evans KE, Kripakaran P, et al. A state-of-the-art review on the application of auxetic materials in cementitious composites. Thin-Walled Struct 2024;196.
[29] Meng Z, Xu Y, Zhou W, Xie J, Savija B. Foamed cementitious composites with 3D-printed auxetic lattice reinforcement: enhancing static and cyclic performance. Compos B-Eng 2025:303.
[30] Yao XH, Liu K, Dong Q, Li XY, Ma CF, Hu N. Tunable and recoverable energy absorption of foam-embedded architected cellular composite material at multiple strain rates. Compos Struct 2024:329.
[31] Liu YZ, Zhao CF, Xu C, Ren J, Zhong JL. Auxetic meta-materials and their engineering applications: a review. Eng Res Express 2023;5(4).
[32] Ren X, Das R, Tran P, Ngo TD, Xie YM. Auxetic metamaterials and structures: a review. Smart Mater Struct 2018;27(2).
[33] Sondagar HD, Kumar S. Experimental investigation on tailoring compressive properties and energy absorption of 3D printed gradient star re-entrant hybrid auxetic structure. Rapid Prototyp J 2025;31(2):379–92.
[34] Novak N, Krstulovic-Opara L, Ren Z, Vesenjak M. Mechanical properties of hybrid metamaterial with auxetic chiral cellular structure and silicon filler. Compos Struct 2020;234.
[35] Hu QF, Lu GX, Tse KM. Compressive and tensile behaviours of 3D hybrid auxetic-honeycomb lattice structures. Int J Mech Sci 2024:263.
[36] Yang HM, Yang L, Zheng XR, Xu SH, Zhang Y. High-performance 3D auxetic metamaterials enabled by multiple auxetic mechanisms. Int J Mech Sci 2025:287.
[37] Luo HC, Gao Q, Zhou JZ, Zhang Y, Bao FL, Chen J, et al. Hybrid honeycombs with re-entrant auxetic and face-centered cubic cells: design and mechanical characteristics. Eng Struct 2025;328.

[38] Yang HY, Qian ZL, Wang JY, Wang JC, Wu SJ, Li ZY, et al. Bifunctional 3D lattice metamaterials for vibration attenuation and crushing resistance. Int J Mech Sci 2025;306.
[39] Tian YQ, Zhang C, Yang L. Additive manufacturing of vibration attenuation and load-bearing integrated metamaterials. Int J Mech Sci 2026:313.
[40] Wu WJ, Liu P, Wang YQ, Kang Z. Design of dual-material lattice structures with compression-torsion bistability. Mater Des 2023:230.
[41] Usta F, Zhang ZN, Jiang H, Chen YY. Harnessing structural hierarchy and multi-material approaches to improve crushing performance of re-entrant honeycombs. J Manuf Process 2023;92:75–88.
[42] Wang K, Chang YH, Chen YW, Zhang C, Wang B. Designable dual-material auxetic metamaterials using three-dimensional printing. Mater Des 2015;67:159–64.
[43] Johnston R, Kazanci Z. Analysis of additively manufactured (3D printed) dual-material auxetic structures under compression. Addit Manuf 2021;38.
[44] Wang WJ, Zhang WM, Guo MF, Yang H, Ma L. Impact resistance of assembled plate-lattice auxetic structures. Compos Struct 2024;338.
[45] Chen M, Chen ZG, Xuan YW, Zhang T, Zhang MZ. Static and dynamic compressive behaviour of 3D printed auxetic lattice reinforced ultra-high performance concrete. Cement Concrete Comp; 2023. p. 139.
[46] Ma WWS, Yang H, Zhao YJ, Li XW, Ding JH, Qu S, et al. Multi-physical lattice metamaterials enabled by additive manufacturing: design principles, interaction mechanisms, and multifunctional applications. Adv Sci 2025;12(8).
[47] Joseph A, Mahesh V, Harursampath D. On the application of additive manufacturing methods for auxetic structures: a review. Adv Manuf 2021;9(3):342–68.
[48] Maskery I, Aboulkhair NT, Aremu AO, Tuck CJ, Ashcroft IA. Compressive failure modes and energy absorption in additively manufactured double gyroid lattices. Addit Manuf 2017;16:24–9.
[49] Wauthle R, Vrancken B, Beynaerts B, Jorissen K, Schrooten J, Kruth JP, et al. Effects of build orientation and heat treatment on the microstructure and mechanical properties of selective laser melted Ti6Al4V lattice structures. Addit Manuf 2015;5:77–84.
[50] Dong H, Wang HX, Hazell PJ, Sun N, Dura HB, Escobedo-Diaz JP. Effects of printing parameters on the quasi-static and dynamic compression behaviour of 3D-printed re-entrant auxetic structures. Thin-Walled Struct 2025:210.
[51] del Toro SF, Crespo-Sanchez J, Ayllón J, Rodríguez-Prieto A, Camacho AM. Mechanical performance of 3D-printed TPU auxetic structures for energy absorption applications. Polym Test 2025:143.
[52] Zhang B, Li YT, Bai Q. Defect formation mechanisms in selective laser melting: a review (vol 30, pg 515, 2017). Chin J Mech Eng-En 2017;30(6):1476.
[53] Liu BQ, Fang G, Lei LP, Yan XC. Predicting the porosity defects in selective laser melting (SLM) by molten pool geometry. Int J Mech Sci 2022:228.
[54] Leary M, Mazur M, Elambasseril J, McMillan M, Chirent T, Sun YY, et al. Selective laser melting (SLM) of AlSi12Mg lattice structures. Mater Des 2016;98:344–57.
[55] Hu QF, Zhang XY, Zhang JJ, Lu GX, Tse KM. A review on energy absorption performance of auxetic composites with fillings. Thin-Walled Struct 2024:205.
[56] Luo YM, He C, Tao Z, Hao J, Xu HH, Zhang Y, et al. A surface-wave seismic metamaterial filled with auxetic foam. Int J Mech Sci 2024;262.
[57] Choudhry NK, Nguyen TK, Nguyen-Van V, Panda B, Tran P. Auxetic lattice reinforcement for tailored mechanical properties in cementitious composite: experiments and modelling. Constr Build Mater 2024:438.
[58] Xie B, Li X, Zhao X, Hu N. Tunable properties and responses of architected lattice-reinforced cementitious composite components induced by versatile cell topology and distributions. Compos Struct 2023:312.
[59] Zhou W, Bol RJM, Zhou YB, Meng ZZ, Xu YD, Xie JB, et al. Reinforcing mechanism of lattice-reinforced cementitious composites: insights into flexural performance and material interactions. Mater Des 2025:256.
[60] Bol RJM, Zhou W, Meng ZZ, Schlangen E, Savija B. Tailored poisson's ratio-reinforced cementitious composites for flexural applications. Cement Concrete Comp; 2026. p. 168.
[61] Chen M, Chen Z, Xuan Y, Zhang T, Zhang M. Static and dynamic compressive behaviour of 3D printed auxetic lattice reinforced ultra-high performance concrete. Cement Concrete Comp; 2023. p. 139.
[62] Chen M, Fang S, Wang GQ, Xuan YW, Gao DW, Zhang MZ. Compressive and flexural behaviour of engineered cementitious composites based auxetic structures: an experimental and numerical study. J Build Eng 2024;86.
[63] Xu Y, Šavija B. Auxetic cementitious composites (ACCs) with excellent compressive ductility: experiments and modeling. Mater Des 2024;237.
[64] Xu Y, Meng Z, Bol RJM, Šavija B. Spring-like behavior of cementitious composite enabled by auxetic hyperelastic frame. Int J Mech Sci 2024:275.
[65] Gan ZH, Zhuge Y, Thambiratnam DP, Chan THT, Zahra T, Asad M. Recent advances in auxetics: applications in cementitious composites. Int J Prot Struct 2022;13(2):295–316.
[66] Gan ZH, Pham TM, Thambiratnam DP, Chan T, Asad M, Xu SQ, et al. High strain rate effect and dynamic compressive behaviour of auxetic cementitious composites. J Build Eng 2024;94.
[67] Ma YX, Zhang Y, Wang P, Liu J, Zhang ZP, Wang SF, et al. Dynamic damage behavior of auxetic textile reinforced concrete under impact loading. J Build Eng 2024:97.
[68] Zhu YZ, Zhang JH, Cai XN, Wang P, Chen XW. Seismic performance of self-centering prestressed concrete frame with auxetic perforated steel plate shear walls. J Build Eng 2025;101.
[69] Khedr M, Elshokrofy H, Pokka AP, Hamada A, Jaskari M, Mustakangas A, et al. Effect of design parameters on auxetic behavior and stiffness of additively manufactured 316L stainless steel. J Mater Res Technol 2024;30:8805–14.
[70] Hamed AA, Asl RB, Rahimzadeh H. Experimental and numerical study on the structural performance of auxetic-shaped, ring-shaped and unstiffened steel plate shear walls. J Build Eng 2021;34.
[71] Wang JJ, Zhu YZ, Cai XN, Wen YX, Wang P. Hysteresis behavior of auxetic perforated steel plate shear walls with elliptical and peanut-shaped cutouts. J Build Eng 2023:79.
[72] Liu JS, Zhang Y, Wei XJ, Jiang WZ, Li Xue M, Qu YC, et al. Mechanical performance of an assembled 3D auxetic hybrid structure under eccentric and axial compression. Eng Struct 2025;344.
[73] Fíla T, Koudelka P, Falta J, Sleichrt J, Adorna M, Zlámal P, et al. Impact behavior of additively manufactured stainless steel auxetic structures at elevated and reduced temperatures. Adv Eng Mater 2021;23(1).
[74] Papadakis L, Avraam S, Mancisidor AM, Loizou A, Evangelou A, Kyratsi T, et al. Laser-based powder bed fusion additive manufacturing and mechanical characterization of 316 L stainless steel auxetic lattice structures. Int J Adv Manuf Tech 2026.
[75] Kong SY, Li BH, Zhu YZ. Experimental and numerical investigation of steel-concrete-steel composite panels with auxetic metamaterials cores subjected to near-field explosion. Structures 2025;81.
[76] Schagen B, Vitalis T, Thoma A, Bhave T, Pacher M, Blank D, et al. Robotic fabrication of structural steel architected auxetic lattices for reinforced concrete confinement. Structures 2026;86:111355.
[77] Zhong R, Ren X, Zhang XY, Luo C, Zhang Y, Xie YM. Mechanical properties of concrete composites with auxetic single and layered honeycomb structures. Constr Build Mater 2022;322.
[78] Zhou HY, Jia KC, Wang XJ, Xiong MX, Wang YH. Experimental and numerical investigation of low velocity impact response of foam concrete filled auxetic honeycombs. Thin-Walled Struct 2020:154.
[79] Tzortzinis G, Gross A, Gerasimidis S. Auxetic boosting of confinement in mortar by 3D reentrant truss lattices for next generation steel reinforced concrete members. Extreme Mech Lett 2022:52.
[80] Luo C, Ren X, Han D, Zhang XG, Zhong R, Zhang XY, et al. A novel concrete-filled auxetic tube composite structure: design and compressive characteristic study. Eng Struct 2022:268.
[81] Yang YF, Zhao XY, Chow CL, Lau D. Enhancing the confinement of steel reinforced concrete using hexagonal auxetic structures. Thin-Walled Struct 2026;218.
[82] Vandadi M, Heidarnezhad S, Pourhaji P, Rahbar N. Integrating 3D-printed auxetic structures for advanced concrete reinforcement. Adv Mater Interfaces 2025;12(17).
[83] Bol RJM, Xu Y, Savija B. Printing path-dependent two-scale models for 3D printed planar auxetics by material extrusion. Addit Manuf 2024;89.
[84] Teng XC, Jiang W, Zhang XG, Han D, Ni XH, Xu HH, et al. A stretchable sandwich panel metamaterial with auxetic rotating-square surface. Int J Mech Sci 2023:251.
[85] Molazadeh S, Hosseini A. Modelling of material behavior for additively manufactured 17-4 PH stainless steel produced by fused filament fabrication. Cirp J Manuf Sci Tec 2024;52:341–65.
[86] Bol RJM, Xu Y, Lukovic M, Savija B. Does printing direction influence the bond between 3D printed polymeric reinforcement and cementitious matrix? Eng Fail Anal 2025;174.
[87] Bol RJM, Savija B. Micromechanical models for FDM 3D-printed polymers: a review. Polym-Basel 2023;15(23).
[88] Pellegrini A, Palmieri ME, Guerra MG. Evaluation of anisotropic mechanical behaviour of 316L parts realized by metal fused filament fabrication using digital image correlation. Int J Adv Manuf Tech 2022;120(11–12):7951–65.
[89] Peng X, Wu SC, Qian WJ, Bao JG, Hu YA, Zhan ZX, et al. The potency of defects on fatigue of additively manufactured metals. Int J Mech Sci 2022:221.
[90] Ramazani H, Kami A. Metal FDM, a new extrusion-based additive manufacturing technology for manufacturing of metallic parts: a review. Prog Addit Manuf 2022;7(4):609–26.
[91] Rosewitz JA, Choshali HA, Rahbar N. Bioinspired design of architected cement-polymer composites. Cem Concr Comp 2019;96:252–65.